Healing and sliding stability of simulated anhydrite fault gouge: Effects of water, temperature and CO_2

Anne M.H. Pluymakers [a,b,*], André R. Niemeijer [a]

[a] HPT Laboratory, Faculty of Geosciences, Utrecht University, Budapestlaan 4, 3584CD Utrecht, The Netherlands
[b] PGP, University of Oslo, Oslo, Norway

ABSTRACT

Anhydrite-bearing faults are currently of interest to 1) CO_2-storage sites capped by anhydrite caprocks (such as those found in the North Sea) and 2) seismically active faults in evaporite formations (such as the Italian Apennines). In order to assess the likelihood of fault reactivation, the mode of fault slip and/or fault leakage, it is important to understand the evolution of frictional strength during periods of no slip and upon reloading (healing and relaxation behavior) and of the velocity dependence of friction of anhydrite fault gouge. Therefore, we performed slide–hold–slide experiments combined with a velocity-stepping sequence using simulated anhydrite fault gouge (>95 wt.% $CaSO_4$). Vacuum-dry and water-wet experiments were performed at temperatures ranging from 20 to 150 °C, and at an effective normal stress of 25 MPa. We also performed tests using dry CO_2, water-wetted CO_2 and CO_2-saturated water as pore fluid, but only at 120 °C. If pore fluid was present, a fluid pressure of 15 MPa was present. Vacuum-dry samples exhibit similar frictional healing to samples containing lab-air, but healing is significantly enhanced in wet samples. Dry samples exhibit velocity-weakening behavior at T ≥120 °C, and wet samples exhibit velocity-strengthening behavior over the full temperature range. The presence of CO_2 does not influence the healing behavior or the velocity-dependence of friction. Samples containing water-wetted CO_2 exhibit behavior similar to wet samples. We infer that the healing in dry samples is controlled by plastic asperity creep (Dieterich-type), possibly through dislocation creep and/or twinning. In wet samples healing is inferred to be controlled by increases in contact area and cohesion by pressure solution. Using a pressure solution rate model to extrapolate healing by contact area growth indicates that the maximum re-strengthening through such a mechanism will only take days to tens of days.

© 2015 Elsevier B.V. All rights reserved.

1. Introduction

For CO_2 storage in geological storage systems, such as depleted gas reservoirs, it is crucial that the storage process will not lead to fault re-activation, since this may lead to an increased likelihood of a) induced seismicity and b) gas leakage (Benson and Cook, 2005; Miocic et al., 2013; Rutqvist et al., 2013). Many natural gas fields (both on- and offshore) currently under consideration for storage of anthropogenic CO_2 are overlain by anhydrite-rich caprock formations, such as the gas fields in the northwest of the Netherlands and North Sea (Geluk, 2000, 2007) and many fields in the Middle-East, including the Qatar fields (Alsharhan and Nairn, 1994; Bai and Xu, 2014). Reservoir–caprock systems are cut and often laterally sealed by faults, which – especially when cross-cutting the caprock – will most likely contain caprock-derived damage and wear material (fault gouge). In order to evaluate if and when faults might be reactivated, possibly diminishing their

sealing capacity by increasing their permeability, it is important to understand how fault strength evolves during periods of zero slip and whether this evolution is affected by the presence of (supercritical) CO_2. Moreover, understanding fault healing behavior is of importance to further our understanding of the seismic cycle in natural faults (Marone, 1998a). An example of anhydrite-bearing faults in a tectonically active setting are the central Apennines in Italy, a well-studied locality for which it has been shown that M ≥6 earthquakes have nucleated in an anhydrite/dolomite sequence (e.g. Barchi and Mirabella, 2009; Collettini et al., 2009; Mirabella et al., 2008).

It is well-established that experimental fault gouges may regain their strength ("healing") (among others Beeler et al.(1994); Bos and Spiers(2002); Dieterich(1972); Marone(1998b); Niemeijer et al.(2008); Olsen et al.(1998); and Yasuhara et al.(2005)) during laboratory simulations of interseismic periods, i.e. periods of zero imposed slip. Since laboratory experiments are typically of short duration compared to natural processes, identification of the deformation mechanisms operating in the experiments is needed to more reliably extrapolate laboratory results to nature. Several different mechanisms for laboratory fault healing have been proposed in literature. In the seminal experimental works in the '70s, it was observed that strengthening

* Corresponding author at: PGP, University of Oslo, Postboks 1048 Blindern, 0316 Oslo, Norway. Tel.: +47 22 85 60 51.
E-mail addresses: A.M.H.Pluymakers@fys.uio.no (A.M.H. Pluymakers), A.R.Niemeijer@uu.nl (A.R. Niemeijer).

increases log-linearly with hold time for bare surfaces as well as for gouges (e.g. Beeler et al., 1994; Dieterich, 1972; Johnson, 1981; Scholz and Engelder, 1976). The log-linearity could be interpreted in the context of rate-and-state-friction (RSF) by time-dependent growth of asperity contacts and hence has been termed "Dieterich-type" healing, although the exact physical mechanism of contact growth was not identified or specified. In later work, it was observed that in the absence of a fluid (i.e. under vacuum or 0% humidity conditions) healing did not occur for various materials, such as interfaces of granite, quartz single crystals, quartzite, Perspex and gouges of quartz and alumina powders (Dieterich and Conrad, 1984; Dieterich and Kilgore, 1994; Frye and Marone, 2002), indicating that, whatever the mechanism responsible, it must be activated by the presence of water, at least at room temperature conditions. At the same time, in the presence of a chemically active fluid, additional mechanisms, such as pressure solution, fluid-assisted neck growth and/or cementation of pores are likely to operate (Bos and Spiers, 2002; Muhuri et al., 2003; Niemeijer et al., 2008; Olsen et al., 1998; Renard et al., 2012; Tesei et al., 2014; Yasuhara et al., 2005). Note that when such fluid-assisted processes are activated, healing is typically at least an order of magnitude larger and does not always obey a (single) log-linear relation to hold time (even showing exponential growth, as specifically noted by Bos and Spiers(2002); and Renard et al.(2012)). Pressure solution (e.g. Lehner, 1995; Pluymakers and Spiers, 2014; Raj, 1982; Rutter, 1983; Spiers and Schutjens, 1990; Weyl, 1959) involves fluid-diffusional transport of material from localities of high stress (i.e. grain contacts) to localities of low stress (see for a review on pressure solution Gratier et al.(2013)). This typically decreases porosity and increases packing density, and may strengthen individual contacts (e.g. Bos and Spiers, 2002). Fluid-assisted neck growth and pore cementation (e.g. De Meer and Spiers, 1999; Hickman and Evans, 1992) are processes that lead to contact strengthening as well, but they do not lead to increased packing density. Note that, in contrast to pressure solution, these processes are not stress-driven, and therefore do not result in shear stress relaxation during hold periods (Bos and Spiers, 2002).

In order to identify which mechanisms are responsible for healing in anhydrite fault gouges, and to determine the effects of periods with no imposed slip ("holds") on the frictional strength and velocity dependence of friction of such gouges, we performed slide–hold–slide experiments followed by a velocity-stepping sequence at 25 MPa normal stress, as may be expected for faults bounding a ~3 km deep gas reservoir. Note that this value is also appropriate for the lower end of the range of stresses expected on the normal faults in the seismogenic Triassic Evaporite layer in the Italian Apennines due to the occurrence of high fluid pressures (Collettini and Barchi, 2002; Trippetta et al., 2013). This series of experiments was performed at temperatures between room temperature and 150 °C under vacuum and water-wet conditions (i.e. no CO_2). At 120 °C, we performed experiments without holds but with an otherwise identical sliding history for comparison purposes. To assess the short-term effects of CO_2 on anhydrite fault gouge healing, we also performed slide–hold–slide experiments in the presence of dry CO_2, water-wetted CO_2 and CO_2-saturated water at 120 °C. The term 'dry' will be used for samples tested either under vacuum or drained to lab-air, 'dry CO_2' will be used for samples exposed to CO_2 only, whereas 'wet' will be used to refer to samples tested in the presence of either liquid water ($\pm CO_2$) or trace water (transported by CO_2). In the following, we report our findings and we will discuss the implications for fault strength recovery in the context of subsurface CO_2 storage reservoirs and for the Italian Apennines.

2. Method

We conducted no-hold (NH) and slide–hold–slide (SHS) shearing experiments on simulated anhydrite fault gouge using a direct shear assembly located inside an externally heated, triaxial vessel which uses silicone oil as a confining medium. We performed SHS experiments on

dry samples connected to a vacuum ("VAC") at 22 °C/80 °C/120 °C/150 °C, as well as on wet samples pressurized with deionized water ("W") at 80 °C/120 °C/150 °C. At our reference temperature of 120 °C we performed both SHS and NH experiments under six different pore fluid conditions, being:

1) Dry samples connected to a vacuum (VAC)
2) Dry samples vented to lab air (D)
3) Samples pressurized with dry supercritical CO_2 (dry CO_2, or DC)
4) Samples pressurized with deionized water (W)
5) Samples pressurized with water-wetted supercritical CO_2 (WC)
6) Samples pressurized with CO_2-saturated water (CW)

All experimental conditions are listed in Table 1. For all experiments the effective confining t $P_{c,eff}$ equals the effective normal stress σ_n^e, where $P_{c,eff} = \sigma_n^e = 25$ MPa. If a fluid was present, a pore fluid pressure of 15 MPa was used. Note that the relative humidity in the Netherlands is approximately 80–90%.

2.1. Sample material

The anhydrite was obtained from core material retrieved from the Hoogeweg 1 well, Overijssel, the Netherlands (courtesy of Shell Global Solutions). It was taken from the Zechstein 1 Anhydrite Member at the base of the Permian Zechstein Formation (Geluk, 2000, 2007), from 2437 m depth. The core material is described in detail by Hangx et al. (2014). It was crushed and sieved to obtain a fraction smaller than 50 μm to simulate natural wear material ("fault gouge") typically found in the principal slip zones in faults (Engelder, 1974). X-Ray Diffraction (XRD) showed the gouge composition to be predominantly anhydrite with minor amounts of dolomite (Appendix A), quantified with ThermoGravimetric Analysis (TGA; detection limit <0.005 wt.%) to be ≤4 wt.%.

2.2. Experimental apparatus and direct shear assembly

Experiments were conducted using a direct-shear assembly (Fig. 1b) mounted in an externally heated, oil-filled, triaxial pressure vessel (Fig. 1a). The apparatus is described in detail by Hangx et al. (2010) and the direct shear assembly is described by Samuelson and Spiers (2012).

The direct-shear assembly consists of two inverted forcing or shear blocks (Fig. 1b; see also Samuelson and Spiers (2012)). They are fitted with pore fluid channels, which lead to a porous stainless steel plate at the shearing interface, which allows even fluid distribution throughout the layer (plate permeability is $3.1 \cdot 10^{-14}$ m²) (Samuelson and Spiers, 2012). The plate surface is grooved to ensure that deformation will take place within the layer of gouge material and not on the interface (see Fig. 1c for groove height and spacing). Water was pressurized using a servopump and pressure was measured using a Jenssen pressure transducer (50 MPa range; resolution ± 0.02 MPa). CO_2 pressure was kept constant using a ISCO 65D pump, with a built-in Honeywell pressure transducer both for control and pressure measurement (150 MPa range; pressure resolution ± 0.00138 MPa).

2.3. Sample assembly and testing procedure

A 1.4 mm thick simulated gouge layer is dry-pressed at 25 MPa in a pneumatic Matra press onto one of the forcing blocks using a custom made steel jig plus top plate. Both ends of the gouge layer are capped by an indium bar of 1 mm × 1 mm × 35 mm (the width of the gouge layer). At the testing conditions, indium is sufficiently soft that it has a negligible effect on the measured shear strength (see supplementary material in Verberne et al.(2013a)). Following placement of the second shear block, the gaps at either end of the gouge layer are lined with Teflon foil (50 μm thick) and filled with soft, commercially available, silicone rubber plugs (Ecoflex 00-10, manufactured by Smooth-on), to

Table 1
List of experiments, conditions and key data.[a]

Sample code	T [°C]	FT [-]	σ_n^e [MPa]	P_f [MPa]	ϕ_0 [-]	ϕ_f [-]	HS	$\mu_{1.68}$ [-]	$\mu_{5.4}$ [-]	β_1	R^2	β_2	R^2	γ	R^2	Trend
Vacuum — effect of temperature																
VACSHS20-1	20	V	25	–	0.30	0.21	1	0.700	0.662	0.0021	0.9716	0.0024	0.7818	0.0107	0.9705	*vs*
VACSHS80-1	80	V	25	–	0.42	0.18	2	0.683	0.596	−0.0004	0.183	0.0025	0.9716	0.0073	0.9731	*vs*
VAC-SHS1	120	V	25	–	0.39	0.07	1	0.674	0.562	0.0015	0.7904	0.0040	0.9754	0.0044	0.8946	*vs/vw*
VACSHS150-1	150	V	25	–	0.37	0.08	1	0.682	0.620	0.0019	0.8773	0.0031	0.9226	0.0076	0.9855	*vs/vw*
Water — effect of temperature																
WSHS80-1	80	W	25	15	0.38	0.21	1	0.625	0.582	0.0143	0.9651	0.0118	0.9094	0.0210	0.9491	*vs*
WSHS-1	120	W	25	15	0.40	0.14	1	0.595	0.427	0.0117	0.8991	0.0143	0.9894	0.0223	0.9815	*vs*
WSHS150-1	150	W	25	15	0.33	0.10	1	0.606	0.521	0.0321	0.9853	0.0298	0.9890	0.0143	0.9828	*vs*
T = 120 °C — effect of pore fluid for samples without water																
DSHS-2	120	LA	25	–	0.45	0.16	1	0.676	0.600	−0.0012	0.3408	0.0019	0.5904	0.0057	0.9830	*vs*
DCSHS-1	120	DC	25	15	0.39	0.23	1	0.671	0.616	0.0010	0.6403	0.0032	0.9753	0.0043	0.9865	*vs/vw*
T = 120 °C — effect of pore fluid for samples containing water																
WCSHS-1	120	WC	25	15	0.43	0.25	1	0.638	0.510	0.0314	0.9549	0.0239	0.9653	0.0182	0.9713	*vs*
WCSHS-2	120	WC	25	15	0.29	0.17	1	0.588	0.485	0.0255	0.9953	0.0228	0.9947	0.0158	0.9947	*vs*
CWSHS-1	120	CW	25	15	0.40	0.15	1	0.590	0.480	0.0170	0.9744	0.0147	0.9802	0.0170	0.9950	*vs*
T = 120 °C — effect of a different hold sequence																
WSHS-2	120	W	25	15	0.41	0.16	3	0.573	0.507	0.0290	0.8700	0.0232	0.8926	0.0156	0.9854	*vs*
WSHS-3	120	W	25	15	0.35	0.05	4	0.611	0.484	0.0383	0.9579	0.0325	0.9743	0.0131	0.9254	*vs*
CWSHS-2	120	CW	25	15	0.37	0.14	4	0.538	0.486	0.0258	0.9636	0.0262	0.9696	0.0157	0.9929	*vs*
T = 120 °C — NH equivalents, which have experienced a velocity-stepping sequence only																
DNH-2	120	LA	25	–	0.52	0.30	n/a	0.672	0.596	n/a						*vs*
VACNH-1	120	V	25	–	0.46	0.31	n/a	0.666	0.608	n/a						*vs/vw*
DCNH-1	120	DC	25	15	0.40	0.25	n/a	0.660	0.620	n/a						*vw*
WNH-1*	120	W	25	15	0.50	0.05	n/a	0.574	–	n/a						*vw*
WNH-2	120	W	25	15	0.54	0.17	n/a	0.575	0.495	n/a						*vw*
WCNH-1	120	WC	25	15	0.43	0.22	n/a	0.580	0.478	n/a						*vw*
CWNH-1	120	CW	25	15	0.38	0.06	n/a	0.600	0.454	n/a						*vw*

[a] Symbols: *T* denotes temperature, *FT* fluid type, σ_n^e normal stress, P_f fluid pressure, φ_0 starting porosity, φ_f final porosity, *HS* hold sequence, $\mu_{1.68}$ the friction coefficient measured at 1.68 mm shear displacement (at 1.1 μms^{-1}), $\mu_{5.4}$ is that measured at 5.4 mm shear displacement (at 1.1 or 0.21 μms^{-1}), β_1 is the best fit healing-rate-per-decade using $\Delta\mu_1$, β_2 is the best fit healing-rate-per-decade using $\Delta\mu_l$, γ is the best fit stress-relaxation-rate-per-decade, and for all three the associated R^2 is listed in the column to the right. V indicates samples are tested under vacuum, W stands for wet, LA for lab air, DC for dry CO_2, WC for wetted CO_2, WC for water-saturated CO_2 and CW for CO_2-saturated water. The different hold sequences are indicated with numbers (see text for explanation). Finally, "*vs*" indicates that a sample exhibited velocity strengthening behavior, while "*vw*" indicates velocity weakening.

accommodate the shear displacement and to prevent the jacket from tearing when a confining pressure is applied. The diameter of the assembly is measured using calipers to within 0.01 mm, and the cylindrical shape is jacketed in a FEP shrink tube sleeve, wrapped in Teflon tape and finally fitted with an EPDM rubber outer jacket. This cylinder is then sealed against the driver blocks using steel wire tourniquets.
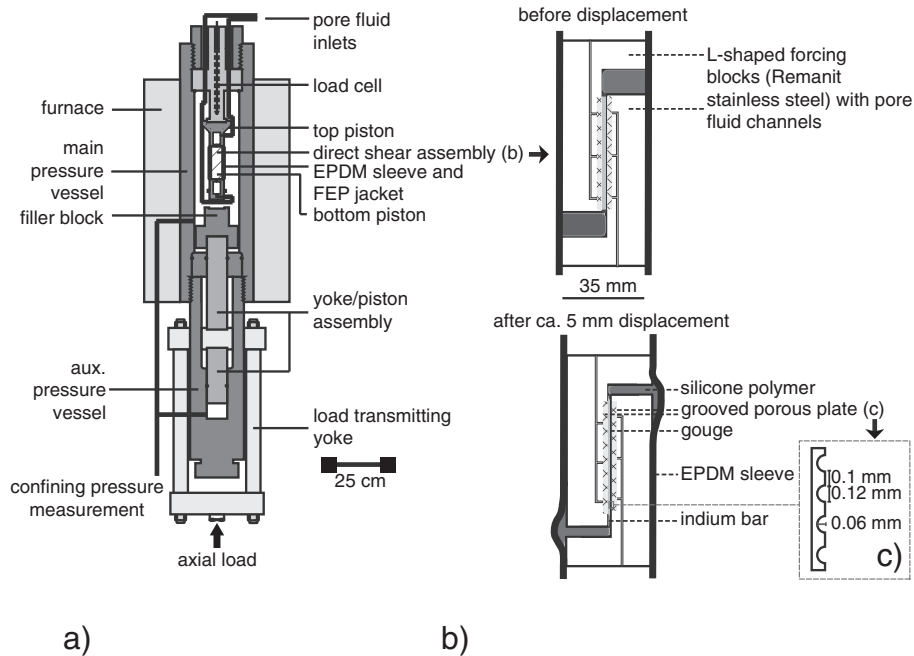
Fig. 1. a) Schematics of the triaxial deformation apparatus (from Hangx et al.(2010)). b) Schematics of the direct shear assembly before and after deformation. c) Close-up of the teeth on the porous plates.

For experiments using CO_2-saturated water as a pore fluid the whole assembly of driver blocks plus cylinder is then placed in a DI water bath, after which the water is drawn into the assembly via a vacuum.

The sample assembly is lowered into the pressure vessel, which is then pressurized to 18 MPa for experiments in which a fluid or CO_2 pressure was used, to ensure $P_c > P_f$ at all times. The pore fluid system is emptied of water and air either through evacuation (in the case of application of water pressure) or through flushing of the pipeline with CO_2 (in the case of application of CO_2 pressure), and then pressurized to 15 MPa. Due to the longer duration of the SHS procedure compared to the NH procedure, the subsequent heating of the pressure vessel took place overnight for SHS experiments (~16 h), whereas for the NH experiments we only heated the vessel for ~4 h that are needed to reach thermal equilibrium. After heating, confining pressure was brought to target pressure, and left to equilibrate for about 30 min. Once pressure and temperature stabilized, the loading ram was brought into contact with the sample assembly at a velocity of 1 μms^{-1}. After a touch point was established and noted, sliding was initiated. For experiments with holds the first hold was performed after ~1.8 mm of displacement, and subsequent holds were performed at 0.3 mm intervals until a total displacement of ~4.9 mm was reached. The standard hold sequence (sequence 1 in Table 1) was 10 s–30 s–100 s–300 s–900 s–1800 s–3600 s–1800 s–900 s–300 s, though for three samples we also imposed hold times up to 27 h (wet and CO_2-saturated water, see Table 1). In Table 1, sequence 2 indicates the shortened standard sequence of 10s–30s–100 s–300 s–900 s–1800s–3600 s, sequence 3 the intermediate hold sequence of 10s–30s–100 s–300 s–900 s–1800s–3600 s–73800 s–3600 s–1800s and sequence 4 the long hold sequence of 10s–30s–100 s–300 s–900 s–1800s–3600 s–14400 s–57600 s–97200 s. At a displacement of 4.9 mm a velocity step to 11 μms^{-1} was performed, with subsequent steps to 1 and 0.2 μms^{-1} at ~0.3 mm displacement intervals. The piston was not halted in NH experiments, i.e. sliding continued at 1 μms^{-1} until a displacement of 4.9 mm, after which an identical velocity-stepping sequence was performed (i.e. 1–11–1–0.2 μms^{-1}). After the final step from 1 to 0.2 μms^{-1}, sliding was continued for another ~0.3 mm for SHS and in NH experiments. The piston was then retracted at 2.2 μms^{-1} until the sample was completely unloaded, and then retracted at a higher velocity (usually 22 μms^{-1}) to its initial position, followed by depressurization of fluid and oil pressure, overnight cooling, and extraction of the sample assembly from the vessel. During cooling the pore fluid system was left open to the atmosphere, effectively drying the wet samples inside the depressurized pressure vessel. Finally, the direct shear forcing blocks were taken apart and chips of the gouge were salvaged where possible. These chips were dried in a 50 °C oven for at least 48 h before further analysis. Selected samples were analyzed by TGA to detect any possible chemical changes (gypsum and/or carbonate formation; sample size 25–65 mg), and after disaggregation by gentle manual stirring, grain size analysis was performed using a laser particle sizer (which uses sonication).

2.4. Data acquisition and processing

Throughout the experiments, internal axial load, piston displacement, confining pressure, temperature, pore fluid pressure and pore fluid volume change (both for water and CO_2) were logged at a frequency of 5 Hz, using a 16-bit National Instruments A/D converter and VI-Logger software. All displacement data were corrected for apparatus distortion using pre-determined polynomial stiffness calibrations. The raw data were processed to obtain shear strength τ (MPa), effective normal stress σ_n^e (MPa), friction coefficient μ (–) and shear displacement (mm). Friction coefficient μ was calculated as τ/σ_n^e, assuming zero cohesion. In order to evaluate the evolution of strength with shear displacement, we have determined the frictional strength both at low displacement ($\mu_{1.68}$ in Table 1) and high displacement ($\mu_{5.4}$ in Table 1). The velocity dependence of friction was analyzed in the framework of

the RSF equations with a Dieterich-type evolution equation ("slowness law") (Dieterich, 1978, 1979):

$$\mu = \mu_0 + a\, ln\left(\frac{V}{V_0}\right) + b\, ln\left(\frac{V_0\theta}{d_c}\right), \quad \text{with} \quad \frac{d\theta}{dt} = 1 - \frac{V\theta}{d_c}, \quad (1)$$

where μ_0 and μ are the friction coefficients (–) before and after the velocity step, respectively, V_0 and V the velocity before and after a velocity step, a represents the magnitude of the direct effect and b that of the evolution effect, θ is a state variable thought to describe the average contact lifetime, and d_c is interpreted to be the slip distance necessary to renew the contact population. Positive values for $(a$-$b)$ describe velocity strengthening behavior, where frictional strength increases with increasing velocity, whereas negative values of $(a$-$b)$ describe the opposite, velocity weakening behavior. The evolution of friction upon a change in load-point velocity can be calculated using Eq. (1) coupled with an equation describing the interaction with the elastic loading frame. To obtain values for the RSF parameters we followed the inversion technique, described elsewhere (e.g. Reinen and Weeks, 1993; Saffer and Marone, 2003). If stick-slip behavior occurred, inversion was not possible and no individual rate and state parameters were obtained. Note that we do not report d_c values, since inversions typically showed large errors. These are attributed to the use of a manually operated gear-box, where changing gears takes slightly different amounts of time and as such encompasses different amounts of displacement. Since the magnitude of a and b should not depend on the displacement over which a velocity-change is imposed, these are considered reliable, especially since fitting the Ruina RSF equation (Ruina, 1983) instead of the Dieterich equation resulted in practically indistinguishable values for a, b and thus of $(a$-$b)$. Furthermore, for selected experiments, the $(a$-$b)$ values were also calculated through use of the steady state method (cf. Pluymakers et al.(2014)), which showed no discrepancies between results obtained with the different methods.

3. Results

Typical curves of shear stress vs. displacement and/or time are shown in Fig. 2. Shear stress increases rapidly with displacement. Most experiments show a small but abrupt drop between 0.1 and 0.6 mm, attributed to alignment of the assembly with the loading ram. Macroscopic yield occurs between 0.6 and 1 mm. Dry samples ($\pm CO_2$ or lab air) are stronger than wet samples $\pm CO_2$ (see Table 1), similar to what has been shown in velocity-stepping direct shear experiments performed on the same material (Pluymakers et al., 2014). Samples containing water-wetted CO_2 as a pore fluid have similar strength to that of fully wet samples (Table 1). Note that the experiments described here are performed on the same anhydrite fault gouge, under the same pressure–temperature conditions, and using the same set-up as the velocity-stepping experiments described by Pluymakers et al. (2014). They performed velocity-stepping experiments only, i.e. without slide–hold–slide sequence. The displacement weakening in the current set of experiments (see Appendix B) has similar characteristics as reported by Pluymakers et al. (2014). It occurs within 1 and 2 mm after yield (Fig. 2a), and it is stronger at lower velocities. The comparison of NH vs SHS experiments shows that there is no systematic dependence on the occurrence of holds, on pore fluid type or on temperature.

In order to describe the strength evolution during and after hold periods, we define a number of strength parameters, illustrated in Fig. 2d. Here, $\Delta\mu_1$ describes the difference between peak strength and sliding strength before the hold period, which is the strength at almost the same load-point displacement. A healing-rate-per-decade β (cf. Beeler et al.(1994); Karner and Marone(1998); Marone(1998b); Nakatani and Scholz(2004); Niemeijer et al.(2008); and Yasuhara et al.(2005)) is constrained by a log-linear least squares regression of $\Delta\mu$ vs. hold time. We indicate the results of this regression for $\Delta\mu_1$ with β_1. Second,
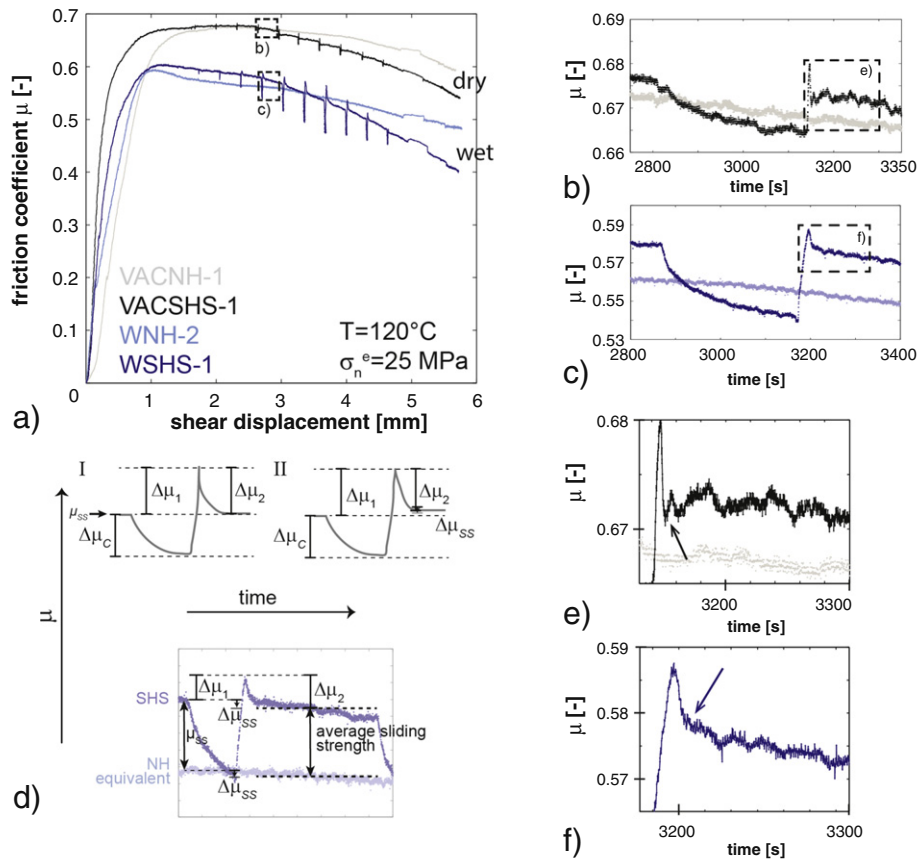
Fig. 2. Typical friction vs displacement curves for two dry and two wet samples. a) Shear stress vs shear displacement. b) Close-up of 1 hold period of 5 min for a dry *SHS* and equivalent *NH* experiments. Note unstable, oscillatory behavior upon re-shear. c) Close-up of 1 hold period of 5 min for a wet *SHS* and equivalent *NH* experiment. Note oscillations after hold period. d) Schematic definitions of the two different healing types, including schematic definitions of steady state strength μ_{SS}, the amount of healing $\Delta\mu_1$ and $\Delta\mu_2$, changes in steady state strength $\Delta\mu_{SS}$, and stress relaxation $\Delta\mu_C$. e) Oscillations after re-shear in dry sample. f) No oscillations in wet sample.

we define $\Delta\mu_2$, which is the difference between peak strength and the average sliding strength after the hold period, which is taken as the average shear stress between 100 and 300 μm after shear has been re-initiated. It took more displacement to reach a new steady state shear strength for experiments with hold periods longer than 1 h, in which cases the average shear stress during sliding was taken between 180 and 300 μm after re-shear. Note that, as a consequence of using the average sliding strength over a distance of 120 or 200 μm, $\Delta\mu_2$ records the total net effect of changes in steady state strength, so both effects of displacement weakening as well as any potential changes in strength resulting from processes occurring during holds. The slope of a log-linear fit of $\Delta\mu_2$ vs. hold time will be indicated with β_2. Third, we define $\Delta\mu_{SS}$ as $\Delta\mu_1 - \Delta\mu_2$, as a measure of changes in steady state sliding strength μ_{SS}. Positive values of $\Delta\mu_{SS}$ indicate that the presence of a hold period leads to a net increase in steady state sliding strength, and negative values indicate a net decrease. However, since this definition involves $\Delta\mu_2$ and experiments displayed significant displacement weakening, this definition for $\Delta\mu_{SS}$ also incorporates displacement weakening effects. Therefore, we also determined a $\Delta\mu_{SS}$ for the *NH* equivalent experiments at 120 °C in order to isolate the effects of displacement weakening and the presence of holds. For an *NH* experiment, $\Delta\mu_{SS}$ was determined using values for sliding strength at the same displacements as for an equivalent *SHS* experiment (i.e. the strength at which the hold would have been initiated, and the average sliding strength over the same displacement interval over which the average strength was determined in each *SHS* experiment). Last, we define $\Delta\mu_C$ as the difference between steady state strength and the value of stress just before re-shear (i.e. the minimum shear stress during a hold), so it is the amount of stress relaxation that occurs during a hold period. The slope of a log-linear fit of $\Delta\mu_C$ vs. hold time will be indicated with γ. These definitions

allow us to distinguish and define two distinct different behaviors, where type I (Fig. 2d) is characterized by $\Delta\mu_1 = \Delta\mu_2$, i.e. $\Delta\mu_{SS} = 0$. A positive $\Delta\mu_{SS}$ is indicative of type II (Fig. 2d) behavior, i.e. $\Delta\mu_1 < \Delta\mu_2$, or $\Delta\mu_{SS} > 0$: the steady state sliding strength after hold is higher than before hold.

3.1. Healing and relaxation

3.1.1. Dry samples ($\pm CO_2$)
A peak strength is typically observed upon re-shear after most hold periods, followed by weakening over a displacement of 50–100 μm until a steady state sliding strength is reached. Occasionally, peak strength is followed by one or two cycles of oscillations in shear strength, the amplitude of which increases with increasing hold duration (see Fig. 2c). Identical experiments without holds (*NH*) showed stable sliding (so no oscillations) within the same displacement interval (Fig. 2c).

Even though dry experiments were performed under vacuum, they all demonstrate measurable strengthening, i.e. measurable $\Delta\mu_1$ values, as do the experiments with lab air and dry CO_2 (see Fig. 3a, b). At the same time, the dependence of $\Delta\mu_1$ on hold time is in some cases poorly fit with a log-linear fit, giving slopes β_1 of -0.0004 to 0.0021, with low coefficients of determination ($R^2 = 0.408$–0.7904, Table 1). Use of $\Delta\mu_2$ instead of $\Delta\mu_1$ to constrain a healing rate gives better log-linear fits for all dry experiments (Fig. 3c, d, Table 1), where $\beta_2 = 0.0024$–0.004 with higher coefficients of determination ($R^2 = 0.5904$–0.9754, Table 1). The discrepancy between $\Delta\mu_1$ and $\Delta\mu_2$ is related to the negative $\Delta\mu_{SS}$ for hold periods of 300 s or longer (Fig. 3e, f). Since displacement weakening is similar in *NH* and *SHS* experiments, we can compare the magnitude of $\Delta\mu_{SS}$ between *NH* and *SHS* experiments. If the negative $\Delta\mu_{SS}$ can be attributed to the presence of hold periods, the *NH*
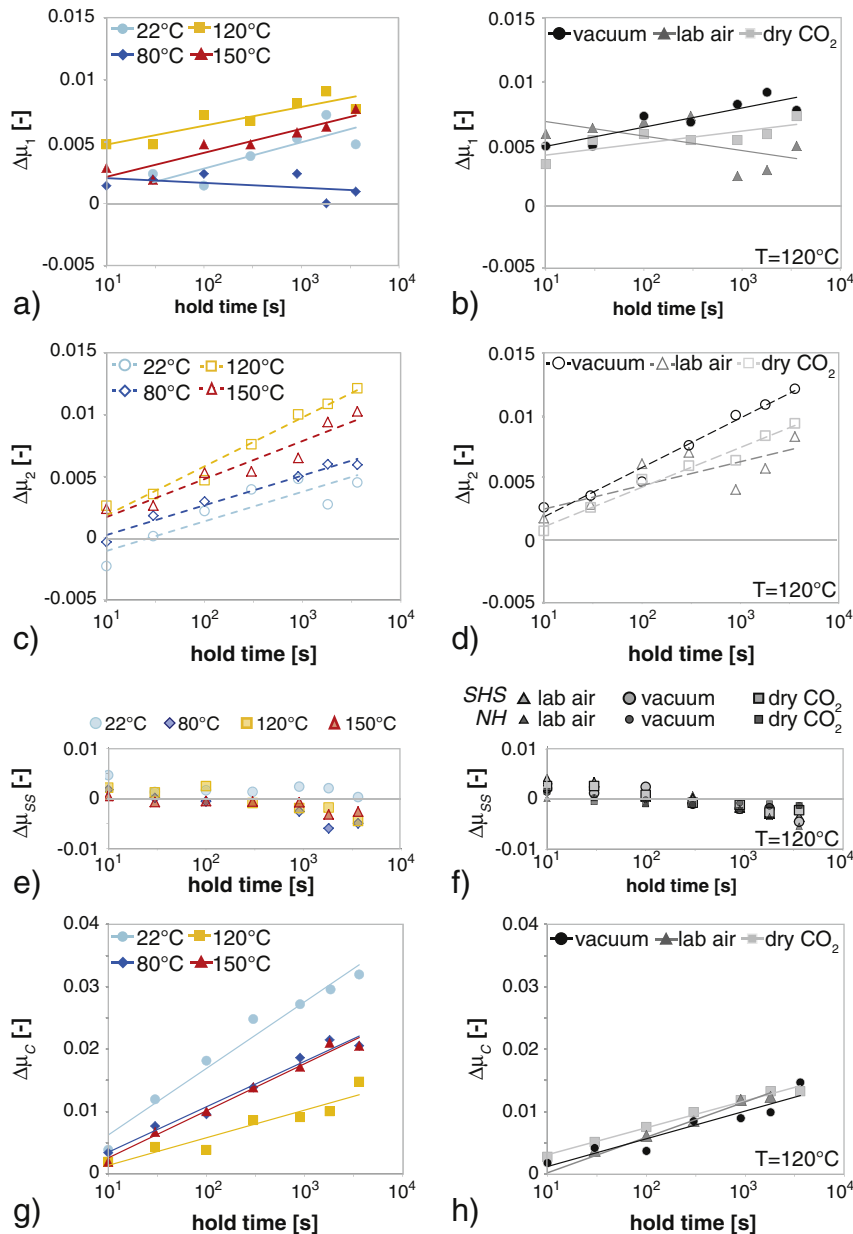
Fig. 3. Healing and stress relaxation for dry samples without (left, vacuum, 22/80/120/150 °C) and with CO_2 (right, 120 °C, lab air, vacuum and dry CO_2.) a–b) $\Delta\mu_1$ vs. hold time [s]. c–d) $\Delta\mu_2$ vs. hold time [s]. e–f) $\Delta\mu_{SS}$ vs. hold time [s]. g–h) $\Delta\mu_C$ vs. hold time [s].

experiments should show different $\Delta\mu_{SS}$ values. However, upon comparison with the equivalent *NH* $\Delta\mu_{SS}$ (at 120 °C, Fig. 3f), this negative $\Delta\mu_{SS}$ is similar between *NH* and *SHS* experiments for hold times below 1 h, indicating that it is probably related to the displacement weakening present in all experiments and not to a change in local steady state sliding strength.

    However, at 60 min, $\Delta\mu_{SS}$ for the *SHS* experiments is more negative than for *NH* experiments, suggesting a slight decrease in steady state sliding strength as a consequence of the hold period. If true, this implies that trends in $\Delta\mu_2$ and β_2, rather than in $\Delta\mu_1$ and β_1, are the most representative for dry samples. β_2 shows a slight linear increase with increasing temperature (Fig. 4, Table 1).

    The amount of stress relaxation $\Delta\mu_C$ depends log-linearly on hold time at all temperatures (Fig. 3g, h), giving $\gamma = 0.0043$ to 0.0107, with a minimum at 120 °C, and the highest value at room temperature (Fig. 4c).

    At 120 °C, we tested one sample using lab-air instead of vacuum (DSHS-2), as well as one sample pressurized with pre-dried CO_2

(DCSHS-1, Table 1). The results both for healing and stress relaxation were comparable to vacuum-dry samples (Fig. 3), i.e. at 120 °C neither lab air nor CO_2 seem to have a measurable impact on dry anhydrite healing and relaxation on the time-scale of these experiments.

3.1.2. Wet samples (±CO_2)

    Healing in wet samples can only be adequately described by a log-linear relation with hold time (Fig. 5) if we consider hold periods of 100 s and longer, since short hold periods are more heavily influenced by measurement error. Doing so leads to a healing-rate-per-decade β_1 of 0.014 to 0.0321 for the samples which have experienced the "standard" *SHS* sequence 1 ($R^2 = 0.8991$–0.9853, Table 1), where β_1 is approximately the same at 80 and 120 °C, and is clearly higher at 150 °C (Fig. 4a). Using $\Delta\mu_2$ instead of $\Delta\mu_1$ gives similar β_2 values, with a similar temperature dependence (Fig. 4b). The β values for wet samples are 10 to 40 times bigger than for dry samples (Fig. 4a and b). The small difference between β_1 and β_2 is reflected by small $\Delta\mu_{SS}$ (Fig. 5e, f). The two experiments with hold times longer than 1 h (WSHS-2 and WSHS-3,
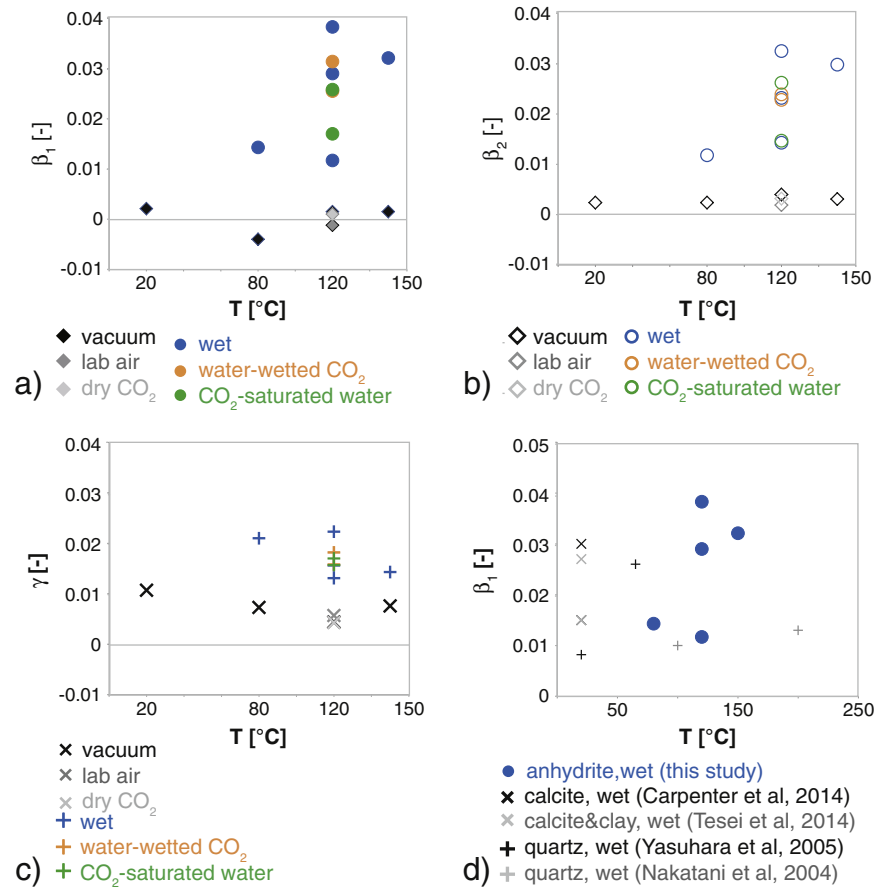
Fig. 4. Trends with temperature a) β_1 vs temperature b) β_2 vs temperature c) γ vs temperature d) comparison between β_1 values from our study for wet samples to β_1 values from other slide–slide–slide studies (Carpenter et al., 2014; Nakatani and Scholz, 2004; Tesei et al., 2014; Yasuhara et al., 2005) in which pressure solution was invoked as a possible deformation mechanism.

sequence 3 and 4 respectively, Fig. 5b, d), show increased β_1 and β_2 compared to the "standard" experiments, with β_1 and β_2 of 0.029–0.0383 ($R^2 = 0.8700$–0.9579) and 0.0232–0.0325 ($R^2 = 0.8926$–0.9743) respectively. As an alternative, since β depends on the hold durations included in the fit, we can fit the complete data-set with a power-law to constrain the healing rate (cf. Bos and Spiers(2002); and Renard et al.(2012)). Doing so for the wet experiments (WSHS-1, WSHS-2 and WSHS-3) gives for $\Delta\mu_1$ vs. hold time an exponent between 0.4541 and 0.5488 ($R^2 = 0.911$–0.9938), and for $\Delta\mu_2$ it gives 0.3084–0.4026 ($R^2 = 0.9849$–0.998), so quite close to an exponent of 1/2. Note that for the long hold periods (60 m and more) there is a clear increase in steady state strength after hold (Fig. 5e, f), i.e. type II behavior (see schematic of Fig. 2d). Moreover, the equivalent $NH \Delta\mu_{SS}$ would predict weakening over similar displacement intervals (Fig. 5f), indicating that the change in steady state strength before and after hold is a result of the presence of hold periods.

The amount of stress relaxation $\Delta\mu_C$ depends log-linearly on hold time over the entire range of hold durations (i.e. compare Fig. 5g to h), resulting in γ-values of 0.0131 to 0.0223 ($R^2 = 0.9254$–0.9854, Table 1). At 80 and 120 °C, values for γ are similar, followed by a clear decrease in γ from 120 to 150 °C (Fig. 4c). Increasing the duration of the longest hold, i.e. going from WSHS-1 to WSHS-2 to WSHS-3, shows that the inclusion of longer hold periods results in smaller γ-values (Table 1), even though the log-linear fit still holds (Fig. 5). The values for γ in wet samples are ~2× those of dry samples (Fig. 4c).

The samples containing water-wetted CO_2 or CO_2-saturated water exhibit characteristics similar to wet samples with respect to both healing and stress relaxation (Fig. 5). For the samples pressurized with water-wetted CO_2, even the small amounts of water dissolved in the CO_2 lead to behavior fully similar to wet samples. The only difference

between samples that are wet only vs. those with CO_2-saturated water is between WSHS-3 and CWSHS-2, which incorporate long hold times (~10^5 s). Here, in contrast to wet experiments WSHS-3, the experiment with CO_2-saturated water did not show an increase in steady state strength after the long hold periods (Fig. 5f).

For water-wet samples the decrease in pore fluid volume indicated continuous compaction during shear and during holds, whereas any anticipated dilatancy effects of re-shear were not visible, probably due to the lack of fine enough resolution on the fluid volume.

3.1.3. Stress relaxation: Dry vs. wet samples

An alternative way of looking at the behavior during the hold periods is to consider it as a stress relaxation experiment on the fault gouge layer. We can calculate the evolution in shear strain rate as a function of time, using the displacement that takes place during a hold period, and the final sample thickness L_f. Note that the displacement data are corrected for the elastic deformation of the triaxial machine, theoretically yielding only the shear displacement of the layer. Strain rate is calculated by applying linear regression analysis to the corrected displacement data stream, such that errors in strain rate remain below 5%. A log–log plot of shear stress vs. shear strain rate gives a measure for the stress sensitivity n of the deformation mechanism(s) occurring during holds, with the underlying assumption that these processes obey a generic rate law $\dot\gamma = A(T) \frac{\tau^n}{d^m}$, where $\dot\gamma$ is the strain rate, $A(T)$ is a constant that depends on temperature, τ is the shear stress with sensitivity n and d is the grain size with sensitivity m. We can calculate n for each hold period separately, or by making a summation of the data for all hold periods in one accumulated displacement vs time dataset, i.e. omitting the displacement that occurs during active shearing. This
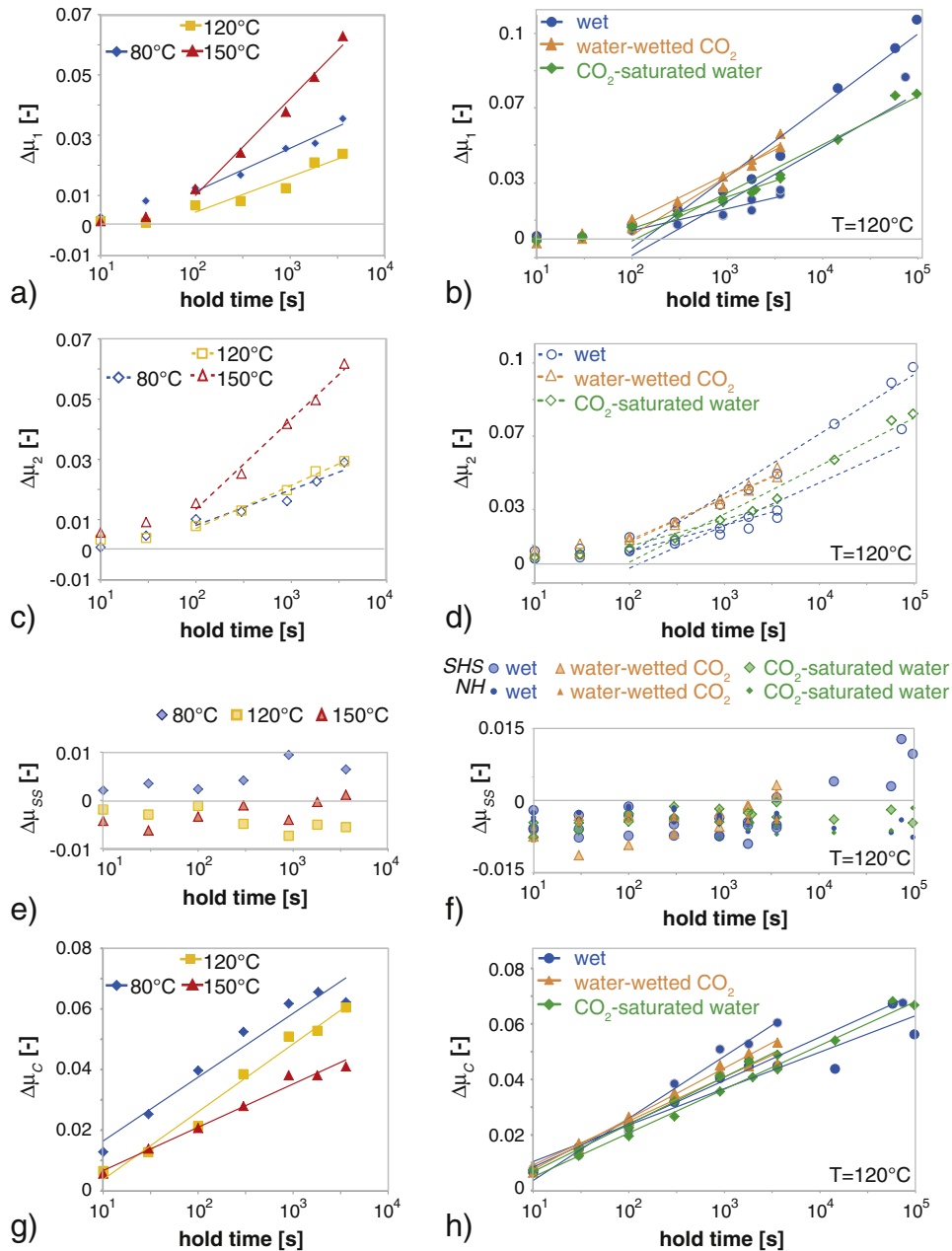
Fig. 5. Healing and stress relaxation for wet samples without (left, wet,80/120/150 °C, *SHS* sequence 1) and with CO_2 (right, 120 °C, wet, wetted CO_2 and CO_2-saturated water) and with CO_2. a–b) $\Delta\mu_1$ vs. hold time [s]. c–d) $\Delta\mu_2$ vs. hold time [s]. e–f) $\Delta\mu_{SS}$ vs. hold time [s]. g–h) $\Delta\mu_C$ vs. hold time [s].

allows us to also use the part of each hold period in which strain rates are too low to reliably calculate strain rate in that segment. Note that this approach is based on the assumption that strain rate in each hold period evolves to a similar trend. Our analysis shows that the dry samples overall show (slightly) larger slopes for the best fit lines (Fig. 6a), though the displacement reached in each hold period was not always sufficient to reliably calculate the strain rate (the displacement can be measured accurately within 8 μm). There are no clear trends with temperature for dry nor for wet samples (Fig. 6b), and there is no clear influence of the presence of CO_2 on the calculated values (Fig. 6c). We assume that the use of the entire displacement vs. time data set leads to the best approximation of an average stress sensitivity, since it mitigates any instantaneous processes that occur upon halting piston motion. Doing so, we find that wet-tested samples show $n \sim$ 0.54–1.3, so on average 0.87, and dry-tested samples $n \sim$ 0.83–1.75, so 1.29 on average (Fig. 6c).

3.2. Rate and state friction parameters

3.2.1. Dry samples ($\pm CO_2$)

For dry samples without CO_2 an increase from room temperature to 150 °C shows a steady decrease in (a-b), resulting in a transition from positive to negative values around 120 °C (Fig. 7a), similar to what has been reported by Pluymakers et al. (in press). At all temperatures, (a-b) is lowest for the lowest post-step velocity (0.2 μms^{-1}). The values of a range between 0.0005 and 0.008 with no systematic dependence on post-step sliding velocity. With respect to temperature, they show a minimum in range and absolute magnitude at 120 °C (Fig. 7b), which coincides with minimum values for the evolution effect b. The b-value for the highest post-step velocity (11 μms^{-1}) is negative at this temperature (Fig. 7c).

Looking in more detail at the results at 120 °C (Fig. 8a), two out of five dry experiments (*NH* and *SHS*) exhibit negative (a-b) for the lowest
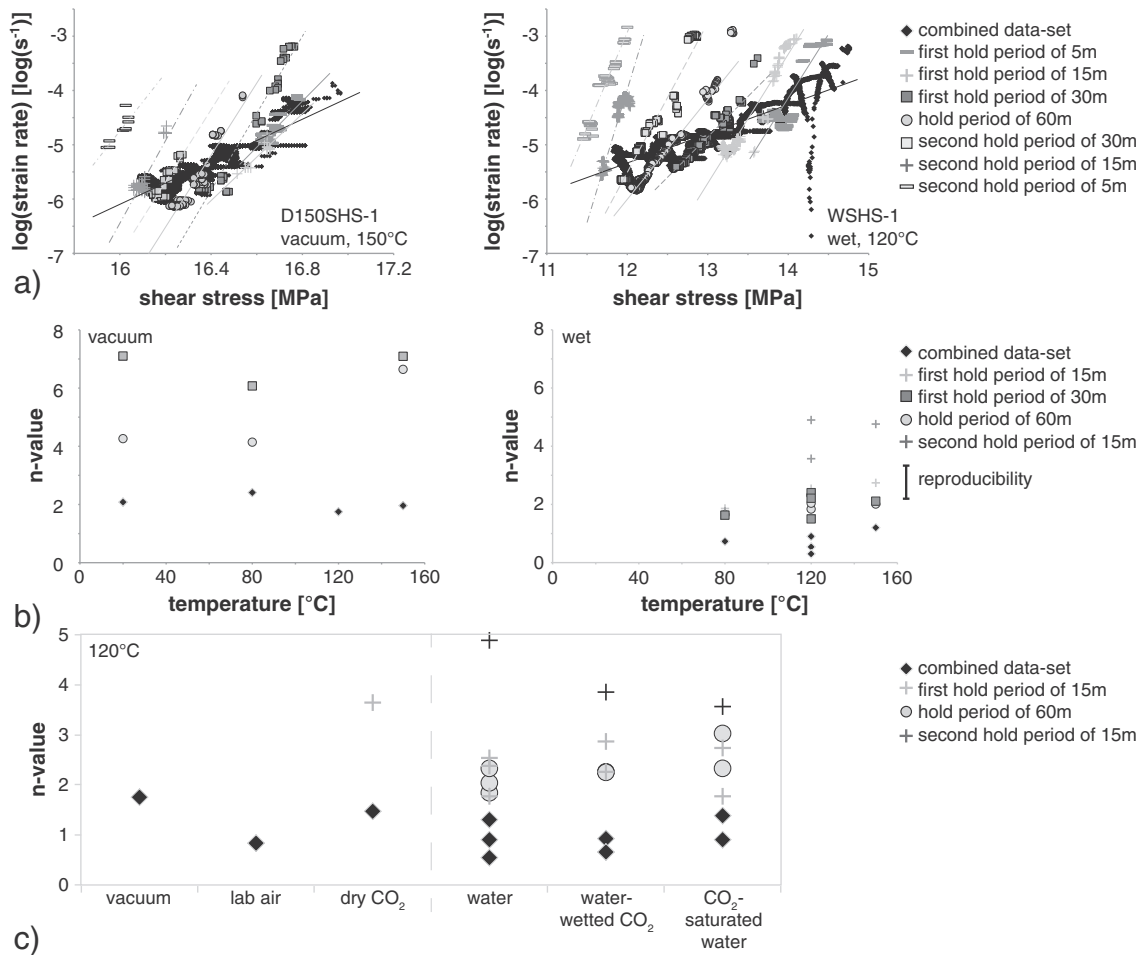
Fig. 6. a) Examples of a dry (D150SHS-1, left) and a wet (WSHS-1, right) experiment for which we plotted the log strain rate during the hold period vs. shear stress, with best fit linear regression lines (of which the slope would be the equivalent n-value). b) n-values for dry (left) and wet (right) experiments as a function of temperature. c) Selected n-values at 120 °C as a function of fluid conditions.

post-step sliding velocity, whereas the other three show values just above zero for the lowest sliding velocities. At 120 °C, a shows no obvious dependence on post-step sliding velocity, whereas b decreases with increasing velocity, and is even negative at the highest post-step velocity. *NH* experiments exhibit a range in (a-b) values from −0.0009 to 0.0028, and *SHS* experiments exhibit a range in (a-b) of −0.0027 to 0.0018, which suggests that the presence of holds slightly decreases (a-b) (Fig. 8a). The magnitude of the direct effect a decreases with the presence of holds as well (Fig. 8b), which could thus be the reason for the decrease in (a-b). The dry experiments DSHS-2, VACNH-1 and the dry CO_2 experiment DCSHS-1 showed unstable stick–slip behavior at the lowest sliding velocity of 0.2 μms^{-1}.

The RSF parameters determined in *NH* and *SHS* experiments using dry CO_2 as a pore fluid showed the same overall magnitude and trends as those described for dry experiments, except that in the presence of CO_2, the presence of holds appears to lead to a small increase in b-values (Fig. 8c), whereas without CO_2 b-values were of similar magnitude. However, comparing this apparent change to the reproducibility of the three dry *NH* experiments shows that the apparent increase in b falls within the range of reproducibility.

3.2.2. Wet samples (±CO_2)

To isolate the effect of temperature on the RSF parameters, we show only the results of wet experiments (no CO_2) with identical slide–hold–slide histories in Fig. 7. At all temperatures, (a-b) values are positive (Fig. 7d) and increase with increasing temperature, whereas the individual parameters a and b both decrease in magnitude. Similar to the

dry samples, samples exhibit the lowest a and b values at high post-step velocities, where at 120 and 150 °C b is negative for the intermediate and high velocities, which results in more strongly positive (a-b).

Comparing *NH* to *SHS* experiments at 120 °C shows that individual a and b values are consistently slightly lower for *SHS* experiments in wet experiments and those with CO_2-saturated water, which, for the lowest sliding velocity, results in more strongly negative b-values in *SHS* than for *NH* experiments. However, because a and b decrease similarly for *NH* to *SHS*, they do not lead to different (a-b) values (Fig. 8).

The experiments with CO_2-saturated water exhibit similar trends to those described for water-wet samples, i.e. (a-b) is the same for *NH* and *SHS* experiments, with decreasing a and b values from *NH* to *SHS*. On the other hand, samples with water-wetted CO_2 do not show any effect of holds on individual a and b values when comparing *NH* to *SHS* experiments.

3.3. Results from post-experimental analyses

Post-experiment TGA analyses of sample chips showed no significant changes in carbonate and/or gypsum content for any of the samples, regardless of pore fluid type.

3.3.1. Laser particle sizer results

The results of the particle size analyses are shown in Fig. 9. Dry pre-pressing of the material does not alter the grain size compared to the loose starting material. For all sheared samples particle size analysis was performed post-experiment, i.e. after unloading, cooling, drying
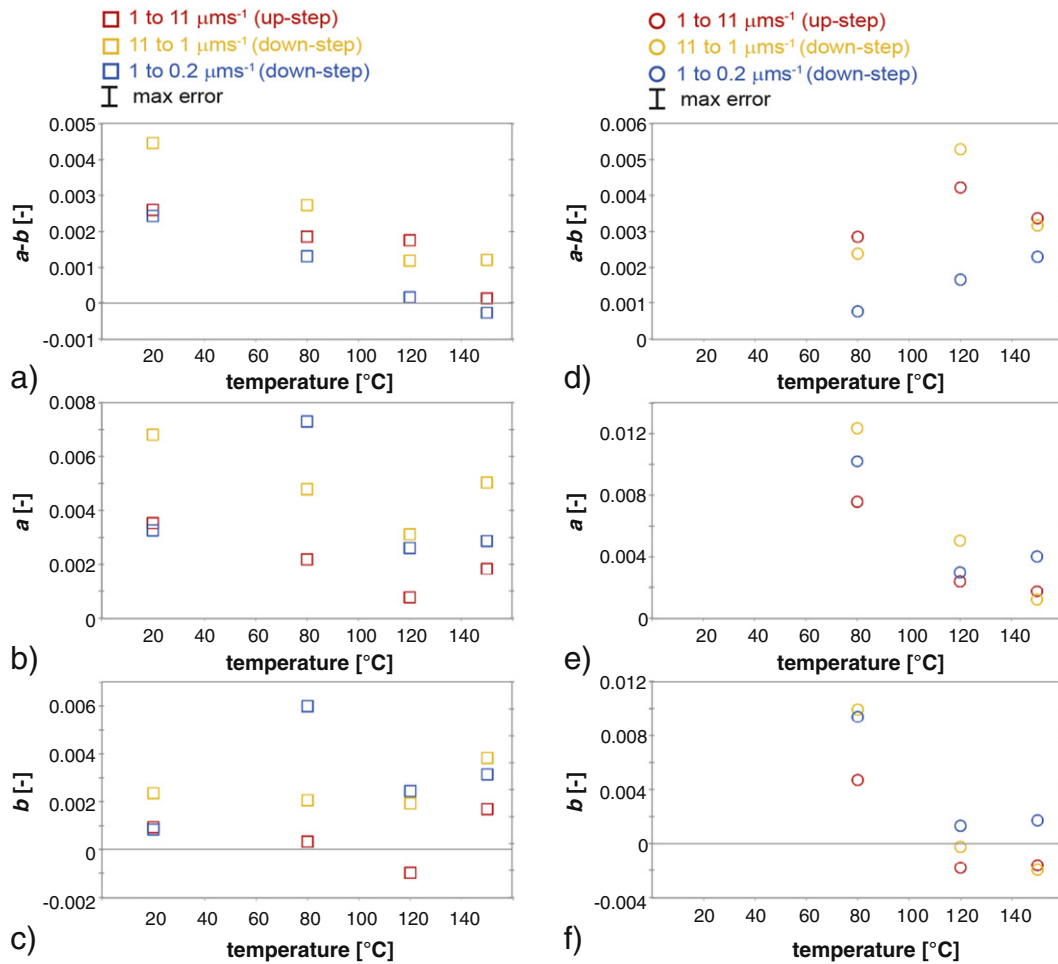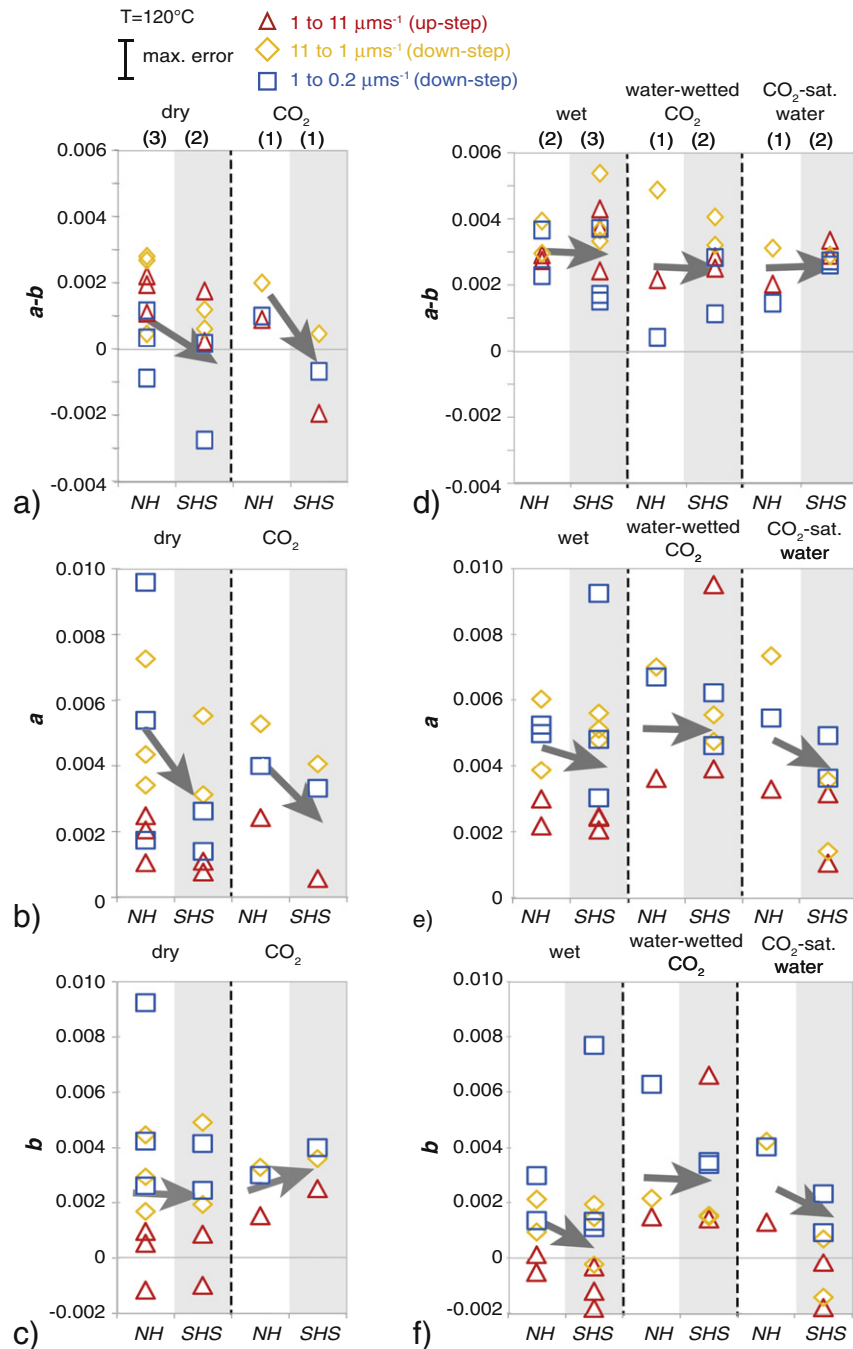
Fig. 7. Rate and state friction parameters for the different velocity steps (Dieterich model) at different temperatures for dry (a–c) and wet-tested samples (d–f). a) (a–b) vs. temperature (°C) for dry samples. b) a-values vs. temperature (°C) for dry samples. c) b-values vs. temperature (°C) for dry samples. d) (a–b) vs. temperature (°C) for wet samples. e) a-values vs. temperature (°C) for wet samples. f) b-values vs. temperature (°C) for wet samples.

and subsequent disaggregation. There are significant changes in the grain size distribution. The *NH* dry sample shows mainly grain size reduction, through an increased percentage of grains smaller than the median and a slight change in the median grain size (from 48 to 36 μm). The post-experimental grain size distribution of the *SHS* dry sample is bimodal, with a secondary peak at 300 μm in addition to an increase in the percentage of fine grains (Fig. 9a). The dry CO_2 samples show more pronounced secondary peaks at 260 μm for the *NH* sample and at 600 μm for the *SHS* sample (Fig. 9a). For all samples containing water ($\pm CO_2$) the primary peak has decreased in height and shifted to the left, indicating significant grain size reduction (Fig. 9b). Only WNH-2 and WSHS-1 do not show a secondary peak. The secondary peak for all other wet(ted) samples ($\pm CO_2$) is at 240 ± 50 μm (Fig. 9b).

3.3.1.1. Secondary Electron Microscopy (SEM) results for dry samples. In general, for samples deformed dry, no obvious differences are found between samples deformed at the different temperatures, nor between samples deformed at 120 °C and different fluid conditions, i.e. lab air (DSHS-2), vacuum (VACSHS-1) and dry CO_2 (DCSHS-1). Samples often separate on fractures in a R1-type Riedel shear orientation upon disassembly. SEM shows R1-type shear zones, though the boundaries are difficult to determine (Fig. 10a). They have meandering orientations and widths of 10–100 μm and are characterized by finer grain sizes and higher porosities than the matrix of the gouge (assuming that post-experimental sample handling has not upset the porosity too much). Occasionally, parallel to the sample margins elongated patches with meandering edges are visible, interpreted to be remnants of a boundary

Y shear bands (Fig. 10a, both at the top and bottom of the zone). It is impossible to confidently estimate the total width of the boundary shears, since we only recovered part of the gouge. Grain-to-grain contacts are sharp, with cracks emanating from contact points (Fig. 10a), which could be correlated to the increase in percentage of fine-grained material as indicated by the particle size analysis. However, the micrographs do not show any indication of clustered grains with a grain size of ~300 μm.

3.3.1.2. SEM results for wet samples. For samples deformed wet, no obvious differences are visible between samples deformed with or without CO_2, neither upon disassembly nor under the microscope. Only some samples separate on R1-oriented fractures upon disassembly, though it is never as obvious as for the dry samples, and there is no systematic dependence on temperature or pore fluid type. SEM shows all but two samples contain R1-type shear zones, which are well developed and characterized by finer grain sizes, with widths below 50 μm (e.g. WSHS-1 in Fig. 10b). Only in samples WSHS-3 (*SHS*-sequence 4, deformed at 120 °C, Fig. 10b) and WSHS150-1 (*SHS*-sequence 1, deformed at 150 °C), the R1 orientation is not visible in any part of the recovered gouge chip. In all samples, parallel to the sample margins, almost continuous elongated patches with meandering edges are visible, interpreted to be remnants of a boundary shear (Fig. 10b). The patches contain sub-micron sized particles. Since we only recovered part of the gouge layer we cannot estimate the full width or evaluate the continuation of the boundary shear. Grain-to-grain contacts are flat, occasionally with cracks emanating from the contact (Fig. 10b). Frequently, grains

Fig. 8. Rate and state friction parameters for the different velocity steps (Dieterich model). At the top the number of experiments in each column is indicated, where each experiment contains 3 velocity-steps. *NH* indicates experiments with no holds, *SHS* indicates the experiments that have experienced holds before the velocity-stepping sequence. a–c) Dry samples, without and with CO_2. d–f) wet samples, without and with CO_2. a) (a–b), dry samples. b) a-values, dry samples. c) b-values, dry samples. d) (a–b), wet samples. e) a-values, wet samples. f) b-values, wet samples.

contain sets of parallel intragranular cracks (Fig. 10b). In WSHS-3, the experiment of longest total duration (~2.5 days), the small grains (<30 μm) frequently show micron-sized indentations (Fig. 10b, indicated with black arrows), whereas these features are more difficult to find in experiments of shorter duration (compare with Fig. 10b).

4. Discussion

We performed direct shear experiments using variable fluid compositions, using both a no hold (*NH*) and a slide–hold–slide (*SHS*) procedure, followed by three velocity steps at similar displacements for the two types of experiments. We investigated the effect of temperature on the frictional and healing behavior of both dry and water-wet samples. At 120 °C we also investigated the effect of CO_2, using dry CO_2, water-wetted CO_2 and CO_2-saturated water. In line with results previously obtained by Pluymakers et al. 2014), we found that dry samples are stronger than wet samples, and that the presence of CO_2 has only a small effect on sample strength. In addition, the rate of re-strengthening during holds (healing-rate-per-decade β) increases 5- to 20-fold when water is present, as does the amount of relaxation (Table 1, Fig. 4a, b). It has been shown previously that fluid-enhanced processes such as pressure solution and subcritical microcracking play an important role in wet anhydrite fault gouges at these temperatures (Pluymakers and Spiers, 2014; Pluymakers et al., 2014). In the
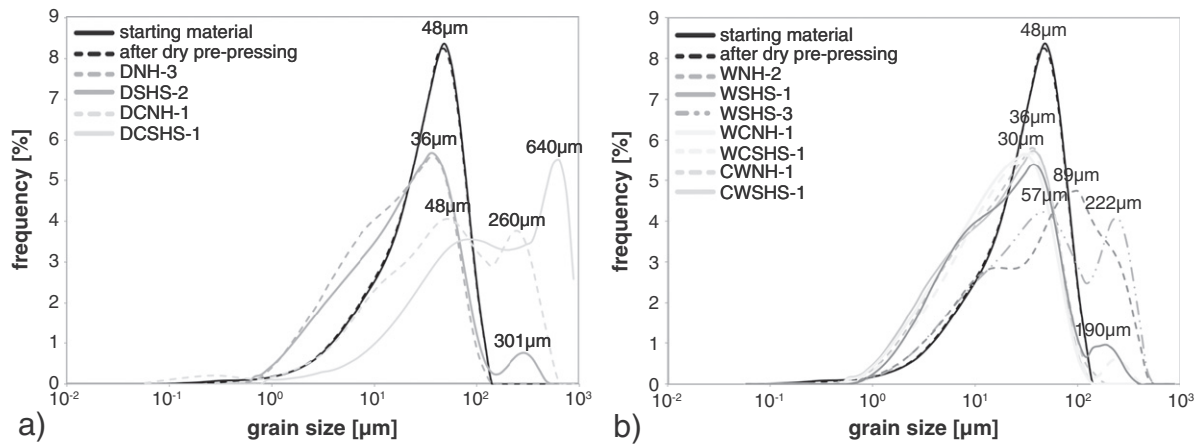
Fig. 9. Laser particle sizer results. Peak grain sizes are indicated above each peak. a) Dry samples without and with CO_2, plus source and pre-pressed material for reference. b) Wet samples without and with CO_2, plus source and pre-pressed material for reference.

following, we will therefore discuss deformation mechanisms active in dry samples separately from those in wet samples, and their effects on stress relaxation, re-strengthening and rate and state friction parameters. We will go on to discuss the implications of these findings for fault strength recovery in the context of reservoir-bounding faults to subsurface CO_2 storage sites and for the major faults in anhydrite/dolomite sequences in the Italian Apennines.

4.1. Deformation mechanisms in dry samples

4.1.1. Effects on strengthening and relaxation behavior

The occurrence of a peak strength upon re-shear after a hold in a friction experiment on gouge is a combination of the changes in contact area, contact strength and the work done against the normal stress (the latter only if porosity changes during the hold) (Marone, 1998a; e.g. Marone et al., 1990; Muhuri et al., 2003; Yasuhara et al., 2005). Previous work on frictional strengthening on a number of different materials has shown that healing does not occur in the absence of water (vapor) at room temperature conditions (Dieterich and Conrad, 1984; Dieterich and Kilgore, 1994; Frye and Marone, 2002). Surprisingly, here we found measurable re-strengthening after hold periods at all temperatures (Fig. 3), where it should be noted that dry samples at room temperature exhibit relatively strong stress relaxation (Fig. 3g) compared to the samples at elevated temperatures. This may be explained by the presence of residual water adsorbed to the grain contacts due to the high relative humidity in the sample preparation room, where the applied vacuum was not strong enough at room temperature to remove all water. At temperatures approaching the boiling point and above (residual), water should become more mobile, and thus easier to remove. It seems thus reasonable to state that only experiments at elevated temperature are fully water-free.

Despite being water-free, these dry experiments still exhibited log-linear time-dependent healing, indicating that a time-dependent increase in the real area of contact (such as envisioned in the RSF framework) may explain this behavior, without invoking changes in porosity or in contact strength. The observation of stress relaxation during the hold periods, combined with the mildly increased values for β_2 going from room temperature to 150 °C (Figs. 3b, 4b) is also consistent with the interpretation of plastic asperity creep generally attributed to "Dieterich-type" healing (Dieterich, 1972; Dieterich and Conrad, 1984; Dieterich and Kilgore, 1994). Comparing our experiments to previous experiments under vacuum-dry but room temperature conditions (e.g. Dieterich and Conrad, 1984; Dieterich and Kilgore, 1994; Frye and Marone, 2002), the main differences lie in the elevated temperature of the experiment, and in the relatively low temperature (~300 °C) at which anhydrite starts to deform in a fully ductile manner

(Dell'Angelo and Olgaard, 1995; Hildyard et al., 2011; Müller and Siemes, 1974; Müller et al., 1981). Experimental work done on compression of anhydrite cylinders indicates that from room temperature up to ~450 °C the main plastic processes are dislocation creep and twinning, with a stress exponent value n of ~1.5–2 for both processes (Müller et al., 1981). A direct comparison between cylinders of low (close to zero) porosity with our porous granular gouges is probably not justified, but it is striking nonetheless that our stress relaxation vs. strain rate curves also indicate $n \sim 1.5$ (Fig. 6c). This suggests that the Dieterich-type asperity creep responsible for the healing found in our vacuum-dry samples might be due to twinning and/or dislocation creep at the highly stressed contacts. Both may lead to healing, through growth of contact areas, increased contact strength or an increased number of contact points (through twinning), however, our data is not sufficient to distinguish between these two deformation mechanisms.

4.1.2. Effects on RSF parameters

The oscillations upon re-shear after a hold seen in the dry samples (Fig. 2) also indicate negative $(a-b)$, where the hold–slide sequence can be seen as a velocity-step. The combination of d_c, $(a-b)$, machine stiffness and normal stress is close to the boundary between frictionally stable and unstable sliding (e.g. Scholz, 2002), and hence causes oscillations. This is not unsurprising, given that the transition from velocity-strengthening to velocity-weakening behavior is observed at 120 °C for our *SHS* experiments, i.e. the same as in velocity-stepping experiments on the same material (Pluymakers et al., 2014). They interpreted the transition to velocity weakening as due to the onset of a time-dependent crystal plastic mechanism, operating at a sufficient rate to compete with (dilatant) displacement-dependent granular flow (cf. Niemeijer and Spiers(2006); Pluymakers et al.(2014)). Our healing data suggest that dislocation creep and/or twinning operate in our samples during the hold periods, which both should become faster with increasing temperature, making it tempting to postulate that the thermally activated process leading to velocity-weakening behavior may be dislocation creep or twinning, similar to what has been proposed for shear-accommodation in calcite gouges (Verberne et al., 2013a,b).

The transition from positive to negative $(a-b)$ at 120 °C should be related to a larger decrease (going from 80 °C to 120 °C) in the direct effect a compared to the decrease (for the same temperature-change) in b. The similarity in trend with temperature for a and b suggests that the activated plastic process influences the magnitude of both. Thermal activation of this process at 120 °C is consistent with the observed increase in a and b between 120 and 150 °C, and also consistent with the observed decrease in b with increasing post-step velocity. For ultrafine
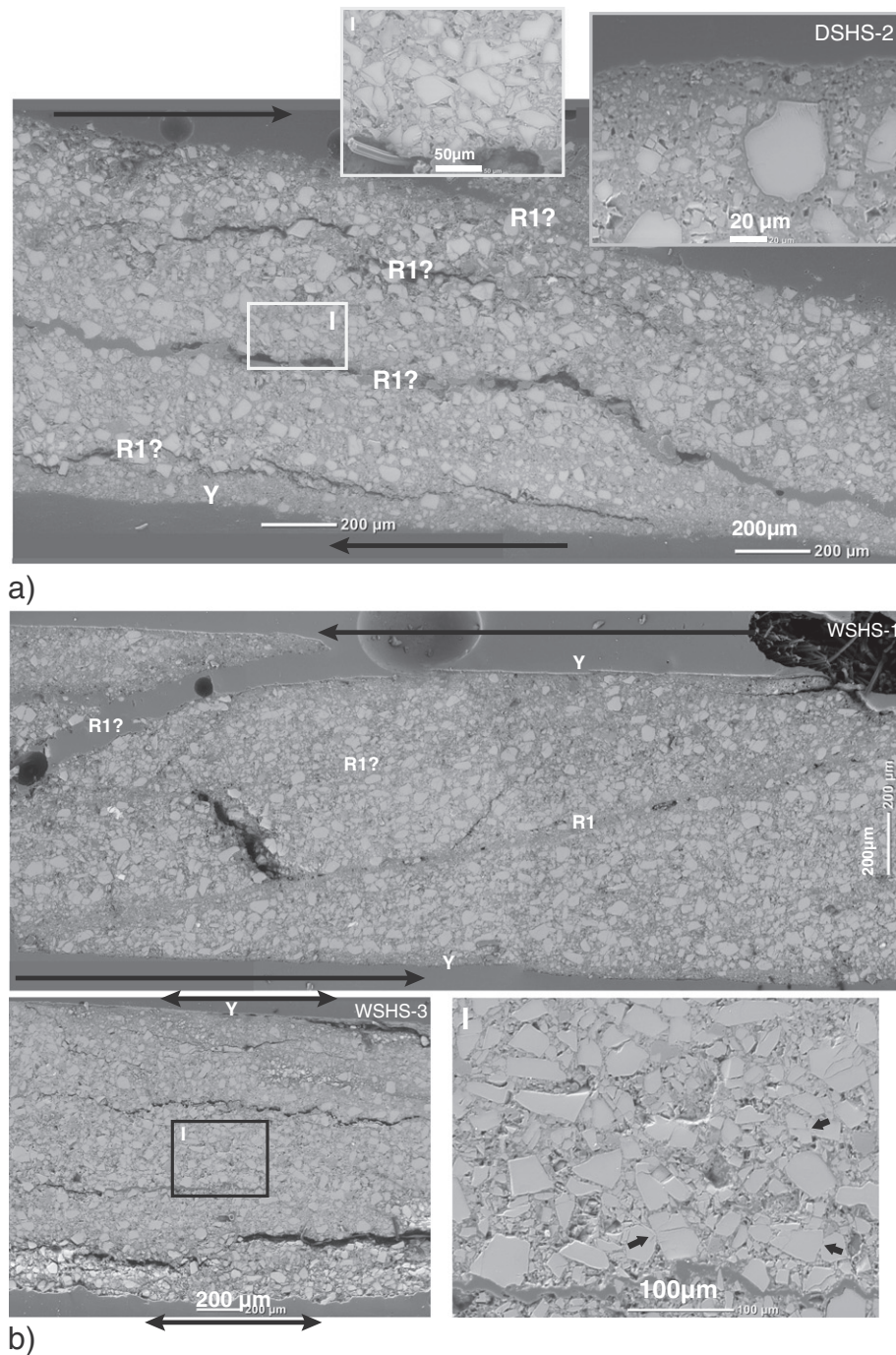
Fig. 10. Back scatter electron images of a) R1-type and boundary shear zones in representative dry sample (120 °C) DSHS-2. Inset shows sharp grain contacts and intragranular cracks, and top right is a close-up of the boundary shear zone, showing grain size reduction. b) R1 and boundary shear zones in representative wet samples (120°) WSHS-1 and WSHS-3. Inset shows flat grain contacts, intragranular cracks, grain size reduction and micron-sized indentations (indicated with arrows).

quartz gouges, Chester and Higgs (1992) reported a clear increase in a with a temperature increase from room temperature to 600 °C, as do Blanpied et al. (1998) from experiments on granite gouges. However, looking at the low temperature data in both datasets, their scatter in a-values is of the same order as what is observed in this set of experiments, implying that to firmly establish any temperature effects on a, a larger range in temperatures and/or velocity-steps should be explored.

The decrease in $(a-b)$ as a result of the presence of holds is the result of a decrease in a while b does not change. Changes in a can be related to changes in 1) in the work done against normal stress through dilatancy (or compaction) needed to reach a new steady state porosity or 2) the

inherent (velocity-dependent) strength of the grain contacts. Since the normal stress is the same for all experiments, the only way to satisfy option 1 would be to assume changes in steady state sliding porosity (and associated changes in gouge volume). It is possible that, as a consequence of continuous compaction during holds, SHS gouges have lower steady state sliding porosities at constant velocity than the NH experiments. However, if this were true, a larger dilatancy would be needed upon a velocity-increase, i.e. implying increased a-values instead of decreased a-values. In contrast, a change in contact strength could be related to an increase in cohesion (through dislocation creep for example), which may also account for the occurrence of a secondary peak in the laser particle sizer data (Fig. 9a), though not for the suggested

decrease in steady state strength. Alternatively, creep during holds may lead to local contact strengthening in the gouge, so that upon re-shear sliding occurs on a smaller, narrower shear zone than the one being active during an *NH* experiments. Since localized deformation has been shown before to be associated with velocity-weakening behavior (for example in Beeler et al., 1996) this could provide a viable explanation for the decrease in (*a-b*) and *a* with the occurrence of holds, as well as provide an explanation for the decrease in steady state sliding strength.

4.2. Deformation mechanisms in wet samples

4.2.1. Effects on strengthening and relaxation behavior

The break in slope at hold periods of ~100 s for the healing in wet samples, as well as the dependence of the log-linear slope on the inclusion of longer hold times in the fits, shows that the data can no longer be fitted with one log-linear line (Fig. 5). This has been seen in many other friction experiments in which water was present (e.g. Bos and Spiers, 2002; Frye and Marone, 2002; Nakatani and Scholz, 2004; Niemeijer et al., 2008; Renard et al., 2012; Yasuhara et al., 2005), especially for those at temperatures which allow for solution transfer processes to occur in the materials investigated. Microstructural models (based on thermodynamics) for porosity-loss of granular aggregates by pressure solution show that contact area grows with time as $t^{1/2-2/3}$, depending on the specific model geometry chosen (e.g. Pluymakers and Spiers, 2014; Spiers and Schutjens, 1990). A similar value is found in models mimicking contacts undergoing neck growth (Hickman and Evans, 1992). An exponent of ⅔ is also specifically mentioned for healing vs. time curves of the *SHS* experiments on wet halite in which pressure solution was active (Bos and Spiers, 2000). As such, it seems that the exponent of ~½ (when using a power-law fit, Section 3.1.2) in our experiments could be an indication for solution transfer processes occurring in our wet samples. Considering that during friction experiments very fine-grained material is produced (Fig. 9) and anhydrite dissolution does not change drastically between 80 and 150 °C, we assume that for all temperatures the pore fluid is locally saturated with anhydrite, i.e. local dissolution and re-precipitation should be possible. Alternatively, it is possible that subcritical microcracking occurs during hold times, which has been shown in compaction experiments to be rapid for anhydrite grains with grain sizes above 50 μm (Pluymakers et al., 2014). However, since there is no systematic difference between *NH* and *SHS* experiments in post-experimental grain size distribution, it seems unlikely that subcritical crack growth plays a dominant role during hold periods (Fig. 9).

The small grain indentations and overgrowths (Fig. 10) observed in WSHS-3 (hold sequence 4, Table 1) combined with the average stress-dependence of strain rate during holds (stress exponent of *n* ~1, see Fig. 6c) suggest pressure solution as a viable deformation mechanism during hold periods. An increase in intergranular cohesion would also explain the increased grain sizes as evidenced by the laser particle analyses (Fig. 9). Assuming pressure solution is indeed the main process operating during holds, it should control healing and relaxation behavior. As such, due to the inverse solubility of anhydrite (Blount and Dickson, 1969), we would expect (slightly) decreasing rates of both with an increase in temperature. This is indeed true for the stress relaxation rate, but for the healing rate we see an increase in healing going from 120 °C to 150 °C (Figs. 4a, b, 5a, c). Even though there is some scatter, when comparing only those samples that have experienced a similar hold sequence, β is highest at 150 °C (Table 1). There are two possible explanations for this. First, other process(es) may be activated at 150 °C that lead to increased strengthening (on top of any strengthening due to pressure solution). Examples of such processes are (fluid-assisted) neck growth, pore cementation and (static) grain recrystallization. Of those, grain recrystallization should also occur in dry samples (assuming fluid doesn't alter recrystallization rates), but the dry sample showed a healing rate 10 times smaller than the wet sample at 150 °C. This leaves fluid-assisted neck growth and pore cementation

(De Meer and Spiers, 1999; Hickman and Evans, 1992) as other possible mechanisms, where our results do not provide enough information to exclude them completely. A second explanation for the difference between stress relaxation and healing rates going from 120 °C to 150 °C could lie in stronger localization on (boundary) shear(s). If this is the case, relaxation of shear stress during holds occurs only in a small part of the gouge, and thus leads to little stress relaxation. However, since the grain size in the (boundary) shear zones is much smaller (see also Fig. 10b), pressure solution should actually operate faster in these high-temperature samples than in the less localized ones at lower temperatures. This could thus lead to an increase in $\Delta\mu$ (at constant hold time) at 150 °C compared to 80 °C and 120 °C, but still lead to a decreased relaxation rate, γ.

For hold durations of 1 h and more, we see a clear increase in steady state sliding strength after the hold period, compared to the strength before the hold period (Fig. 5e, f). Delocalization is typically associated with an increase in shear strength (e.g. Beeler et al., 1996), but seems unlikely when taking the microstructures into account. A more likely explanation is that pressure solution has led to increased contact cohesion, effectively welding grains together in larger clumps. Upon re-shear, these aggregated clumps are then forced to act as one grain, thereby effectively increasing the grain size and contact area, leading to an increase in supported shear stress (cf. Yasuhara et al.(2005)). This requires contact cohesion to be high enough to withstand re-shear, which seems likely, since our laser particle size analysis indicates clumping of grains (Fig. 9). Significant strengthening through healing by pressure solution has been shown previously to occur in fractured sandstones (Tenthorey and Cox, 2006; Tenthorey et al., 2003), where it was attributed to increased cohesion as well.

Invoking pressure solution as the main deformation mechanism controlling healing and stress relaxation in wet samples may also explain the similarity of trends for samples pressurized with water-wetted CO_2. Our reasoning is as follows. CO_2 is only capable of taking up very small amounts of water (Duan and Sun, 2003) before it is saturated with water, and for the amount of CO_2 present in our pore-fluid system (~100 ml) only 1 to 2 ml would suffice. It is very likely that the alternation of dry and wet experiments in the vessel has led to such small amounts of water in the system, which would have easily dissolved into the CO_2, leading to (near-)complete saturation (Duan and Sun, 2003). Furthermore, it has also been shown that forsterite grains in contact with water-bearing CO_2 (respectively 47% and 81% of water) developed a 0.1 nm-thick water film on the grain surface. Moreover, at 95% saturation and more, water films were found with thicknesses of nanometers and more (Kwak et al., 2010; Loring et al., 2011). This suggests that in the samples pressurized with water-wetted CO_2, nanometer-thick water films are likely to be present, coating the grains. As long as there is a fluid film present on the grain contact, pressure solution will proceed (e.g. Spiers et al., 2004). The combined product of diffusion coefficient times fluid film thickness for anhydrite is assumed to be 10^{-20} m³ s⁻¹ (cf. Pluymakers et al.(2014)) and assuming the diffusion coefficient for anhydrite compares to that of calcite (10^{-10} m² s⁻¹ (cf. Zhang et al.(2010))), the fluid film thickness required for pressure solution to proceed in anhydrite will be indeed ~0.1 nm. This indicates that our samples pressurized with water-wetted CO_2 should be capable of deforming by pressure solution, and this, in turn, would explain why these samples showed identical behavior to the water-wet samples.

4.2.2. Effects on RSF parameters

Our (*a-b*) values for wet samples showed a slight increase to more marked velocity-strengthening with a temperature increase from 80 to 150 °C (Fig. 7), and showed no measurable differences between *NH* and *SHS* (Fig. 8). Pluymakers et al. (2014) found, in a similar temperature range, mostly positive (*a-b*) values and a few negative values, with a hint of a possible transition to more negative (*a-b*) at temperatures just above 150 °C. Our samples are slightly thicker, and have

experienced a different history than the samples in the aforementioned study. Our *NH* experiments also experienced only a velocity-stepping sequence, and showed only velocity-strengthening behavior as well. Therefore it seems likely that the small differences in the gouge thickness are responsible for the increased stability of sliding in this study, similar to that previously shown for granite gouges by Byerlee and Summers (1976).

We observed some trends for individual *a*- and *b*-values. With increased temperature and velocity, both *a* and *b* decrease, but the total (*a-b*) remains at the same level, indicating that they are both similarly influenced by the same process(es), inferred to be pressure solution (cf. Pluymakers et al.(2014)). With respect to *a* only, to explain our healing results, we inferred that at 150 °C pressure solution is mainly active in a highly localized (boundary) shear. If deformation is accommodated in a smaller gouge volume, it may be expected that dilatancy upon a velocity-step will thus also be smaller (cf. Marone et al.(1990)). This could also explain the observed decrease in *a*-values. Scuderi et al. (2013) have shown for velocity-stepping experiments on wet anhydrite gouges that dilatancy increases going from room temperature to 75 °C (normal stresses 10 to 30 MPa). An increased dilatation would lead to increased values of *a* (e.g. Marone et al., 1990). This would imply that for wet anhydrite gouges, going from room temperature to 150 °C, *a* would first increase to 80 °C, and then decrease. Since we have no measurement of dilatation, we cannot confirm the inference made by Scuderi et al. (2013) that *a*-values change by the changing dilatational behavior.

With respect to the evolution effect, it decreases such that it is even negative at 120 °C and 150° for the two highest velocities, in *NH* and in *SHS* experiments. In general, negative *b*-values are fairly common and have been found for phyllosilicates as well as for non-phyllosilicate materials, often for experiments performed under hydrothermal conditions (Blanpied et al., 1998; Ikari et al., 2009; Marone and Cox, 1994; Niemeijer and Collettini, 2013; Niemeijer and Vissers, 2014; Weeks and Tullis, 1985). Ikari et al. (2009) speculated that negative *b*-values may be related to dilatant mechanisms unrelated to porosity, though exactly how that would correlate to our experiments would remain too speculative to include here.

4.2.3. Comparison with model predictions

To further test for the role of pressure solution, we can calculate the theoretical amount of re-strengthening $\Delta\mu_{total}$ due to the increase in contact area associated with porosity loss by compaction via pressure solution. In the following paragraph, we calculate the combined effect of two components: (1) contact growth by pressure solution, $\Delta\mu_{PS}$, and Eq. (2) the dilatancy that occurs upon re-shear, $\Delta\mu_{dil}$ (e.g. Marone et al., 1990; Niemeijer et al., 2008). Note that such a model does not include a possible increase in cohesion, nor does it account for other deformation mechanisms that may be active in the gouge. However, these calculations allow us to evaluate 1) the possibility of pressure solution controlling the healing and 2) the maximum extent of healing that contact growth by pressure solution could produce. To model $\Delta\mu_{PS}$, we used the rate-expression for diffusion-controlled pressure solution in a system of cubic close packed spheres, as derived by Pluymakers and Spiers (2014). It is based on the same approach used by Rutter (1976) and Spiers et al. (2004), and is fully equivalent to the expression used by Pluymakers et al. (2014):

$$\dot{\varepsilon} = \frac{4\pi ADSC_s Z}{Fd^3}\left[exp\left(\frac{\sigma_n^e \Omega Z}{RT}\frac{q}{F q-2\phi}\right)-1\right]\left(\frac{q}{q-2\phi}\right) \tag{2}$$

in which $\dot{\varepsilon}$ is the strain rate, *A* is a geometric constant with value 6, *DS* is the product of diffusion coefficient *D* and mean grain boundary fluid thickness *S* (m³ s⁻¹), C_s is average solubility of solute in the grain boundary fluid (m³m⁻³), *Z* is the coordination number, which can be

taken as 6, *F* is a geometric factor with value π, Ω is the molar volume of anhydrite (mol m⁻³), *d* is the grain size (m), *R* is the gas constant (J mol⁻¹ K⁻¹), *T* is the temperature (K), *q* is a geometric constant, close to 1 (see also Pluymakers and Spiers(2014)) and ϕ is the porosity (dimensionless). This can be coupled with the formulation relating contact area and porosity (Pluymakers and Spiers, 2014):

$$a_c = \frac{Fd^2}{Z}\frac{q-2\phi}{q} \tag{3}$$

Using Eqs. (2) and (3), we can model the healing due to contact growth ($\Delta\mu_{PS}$), by use of the ratio between grain contact area before (a_{c0}) and at the end of the hold (a_c), i.e. $\Delta\mu_{PS} \sim (a_c/a_{c0} - 1)$ (cf. Niemeijer et al.(2008)). To calculate an initial strain rate, we insert an assumed steady state sliding porosity in Eq. (2) (which also gives our assumed initial contact area) plus the values listed in Table 2. This initial strain rate leads to a compaction strain in the gouge volume, with which a new aggregate geometry and thus a new porosity can be calculated. These can be used to calculate a new strain rate, contact area and thus $\Delta\mu_{PS}$ in each time-step. Note that the approximations to determine porosity in the model of Pluymakers and Spiers (2014) break down at 5%, which is thus chosen to be the porosity at which healing is "complete". Note as well that natural fault gouges may have porosities lower than 5%, the porosity below which the pressure solution model is no longer valid. This number is related to the assumed geometry of spherical particles in a cubic close packing (cf. Pluymakers and Spiers(2014)). The highest input porosity is chosen to be 20%, as was determined to be the maximum porosity at the end of direct shear experiments on granular calcite using a similar direct-shear set-up (Verberne et al., 2014). The highest grain size is taken to be 20 μm, to be representative of the bulk grain size (Fig. 9). Now, the dilatancy that occurs upon re-shear, $\Delta\mu_{dil}$ needs to be calculated from our modeled porosity change due to pressure solution, since our experimental set-up does not provide a direct way to measure dilatation upon re-shear. From a combined energy and entropy balance for a representative unit of fault rock volume during deformation (see for details Bos and Spiers(2000, 2002); Lehner(1995); Niemeijer and Spiers(2006, 2007); Niemeijer et al.(2008)), it can be shown that the measured friction is $\mu = \tau_x/\sigma_n^{eff} - d\varepsilon_v/d\gamma$ (rewritten from Niemeijer et al.(2008)). In this expression τ_x represents the contribution in measured peak friction of all energy dissipation and storage processes in the gouge. The ratio $d\varepsilon_v/d\gamma$ is the contribution to the measured friction by dilatancy, so $\Delta\mu_{dil} = d\varepsilon_v/d\gamma$, i.e. the change in volumetric strain $d\varepsilon_v$ over the change in shear strain $d\gamma$. From Eqs. (2) and (3), we can calculate the change in volumetric strain as $d\varepsilon_v = -\frac{\Delta\phi}{\phi}$, i.e. from the modeled change in porosity (i.e. from Eq. (2) and (3)), and to estimate dγ from our experimental data we take the average shear strain needed upon re-shear before the peak friction is reached (the values are listed in Table 2).This approach provides us with an upper bound of the total dilatation possible.

Combining our modeled values for $\Delta\mu_{PS} + \Delta\mu_{dil}$ gives the results shown in Fig. 11 for the different temperatures at which our wet experiments are performed. Especially at 80 °C and 120 °C the model predictions may explain (part of) the observed $\Delta\mu$ values, especially considering the scatter between the different experiments and the uncertainties in steady state sliding porosity and the average grain size. Comparison between the middle and right column in Fig. 11 shows that the even maximum possible contribution of $\Delta\mu_{dil}$ is still relatively minor in most cases, up to 0.02. This implies that if the porosity reduction during hold is not fully recovered upon re-shear (i.e. as also suggested by the results of Scuderi et al.(2014)), the trends of the presented model may be more similar to Fig. 11c, f and i. Regardless of the inclusion of $\Delta\mu_{dil}$, the model also approximately reproduces the exponential dependence of re-strengthening on hold time reasonably well, especially at long (>10²–10³ s) hold times. This implies that for

Table 2
Values of parameters and variables used in applying the diffusion-controlled pressure solution model of Pluymakers and Spiers, 2014 to estimate healing by pressure solution within our fault gouge.

Symbol	Definition	Typical value	Source & additional information
A	Geometric constant	6	Assuming a simple cubic pack of grains
C_s	Anhydrite solubility		
	at 80 °C [$m^3\ m^{-3}$]	$6.3\cdot10^{-4}$	Blount and Dickson (1969)
	at 120 °C [$m^3 m^3$]	$1.8\cdot10^{-4}$	
	at 150 °C [$m^3\ m^{-3}$]	$1.1\cdot10^{-4}$	
DS	Product of diffusion coefficient D and mean grain boundary fluid thickness S [$m^3\ s^{-1}$]	10^{-20}	Pluymakers and Spiers (2014); Pluymakers et al.(2014)
F	Grain shape factor	π	General value for simple cubic packed spherical grains
ϕ	Porosity [–]	0.075–0.20	Assumed range of porosity in a shear band (see also Verberne et al.(2014))
q	Geometric constant	0.97	Pluymakers and Spiers(2014)
R	Gas constant [$J\ mol^{-1}\ K^{-1}$]	8.314	(e.g. Chang, 2000)
Z	Coordination number	6	General value for simple cubic packed spherical grains
Ω	Molar volume of anhydrite [$m^3\ mol^{-1}$]	$4.6\cdot10^{-5}$	Hummel et al.(2002); Thoenen and Kulik(2003)
Variables			
d	Grain radius [μm]	5–20	From particle sizer data
σ_n^e	Effective normal stress [MPa]	25 or 50	Assumed value
T	Absolute temperature [K]	353, 393 or 423	80 °C, 120 °C or 150 °C
$d\gamma$	Change in shear strain between the end of the hold and peak strength	$13\cdot10^{-6}/1\cdot10^{-3}$ $15\cdot10^{-6}/1\cdot10^{-3}$ $17\cdot10^{-6}/1\cdot10^{-3}$	From the results obtained at 80 °C at 120 °C at 150 °C

shorter hold times contact growth by pressure solution in the bulk gouge is too slow to contribute significantly to the re-strengthening seen in our gouges, which is not unsurprising. Even in rock salt, a material in which pressure solution is much faster, it is not fast enough to explain re-strengthening for hold times below 300 s (Niemeijer et al., 2008). The modeled results provide particularly good fits at 80 °C, the temperature at which Pluymakers et al. (2014) performed compaction experiments, in which pressure solution was inferred to be the dominant deformation mechanism. A significantly smaller grain size is needed at 150 °C to bring the modeled curves close to the data. This implies that pressure solution in the bulk gouge is not fast enough to explain the observed healing, and that other explanations need to be invoked, such as that the healing behavior may be controlled by the fine grains present in the localized (boundary) shear zones, as was suggested by the contrasting temperature dependence of β and γ (Fig. 4).

4.3. Implications for CO_2 sequestration

We set out to better understand mechanisms of fault healing of simulated anhydrite fault gouges under in-situ reservoir conditions, to understand the implications both for induced seismicity in a CO_2 sequestration scenario, as well as for natural seismicity in evaporite terrains. The reactivation of (CO_2-) reservoir-bounding faults would involve reactivation of faults with a complex history, which we have tried to simulate by comparing results for sliding strength (Fig. 2, Appendix B) and velocity dependence of friction (Fig. 8) for experiments with a NH vs. SHS history. Our results show that simulated anhydrite fault gouge will exhibit time-dependent healing (i.e. fault creep) under a shear stress, especially if water is present (see the comparison between dry and wet samples in Fig. 5) and given sufficient time. As is shown in Fig. 6, during the hold periods, i.e. moments without driving velocity, there are still minor amounts of slip. In the long term, these may lead to a change in fault strength (as observed for wet samples) and sliding stability (as observed for dry samples). The strong fault healing behavior observed in wet samples is thought to favor repeatable slip instability, since it is prerequisite to a cyclical stress buildup in rocks.

Furthermore, when a natural, mature anhydrite-bearing fault is aseismically or seismically reactivated as a consequence of fluid injection (or extraction), it may have a higher initial strength compared to the steady state strength of simulated fault gouges with little to no cohesion (such as reported by Pluymakers et al.(2014); or Scuderi et al.(2013)). If, as suggested by use of the model above, this strength change is assumed to be solely due to an increase in contact areas due to pressure solution, there should be a maximum contact area at which the driving force for pressure solution becomes too low to lead to further growth. We can use the Eqs. (2) and (3) to obtain an estimate for the time-scale on which this maximum contact area is reached. We will assume that fault healing through contact growth by pressure solution is no longer possible at a porosity of 5% (the porosity at which Eq. (3) is no longer valid (Pluymakers and Spiers, 2014)). The values for the all parameters and variables of the model are listed in Table 2. To investigate the effect of grain size on fault healing, we assume that the initial porosity of the fault gouge is 20%, a value reported for experimental slip zones in calcite (Verberne et al., 2014). Estimating the true in-situ porosity is unfortunately not possible in this set-up, and using this value of 20% will thus help constrain a maximum estimate for the duration until complete fault healing is achieved for different grain sizes (Fig. 11g).Natural fault zones may show lower porosities than the 20% reported by Verberne et al. (2014), and therefore we explore a range of porosities in Fig. 11h. Here we chose a fixed grain size of 10 μm, to ensure that the output of the model reflects a maximum expected duration. Using these assumptions and with this range of parameters, our model calculations show that fine-grained anhydrite fault gouges will reach a porosity of 5% within tens of days after a reactivation event, rather than years (Fig. 11g and h). As to be expected, finer grain sized material leads to shorter total duration, as does a lower initial starting porosity. The recurrence times of large (M ≥ 6) magnitude earthquakes in the Italian Apennines, constrained by field evidence, is on the order of 2000 to 5000 years (Cello et al., 1997; Galli et al., 2008; Palumbo et al., 2004; Pantosti et al., 1993). Assuming recurrence interval scales according to the Gutenberg–Richter law, this means that smaller events will still have recurrence times of centuries to decades. Porosity-loss and associated re-strengthening of anhydrite gouges occur much more rapid than this, which shows that it is unlikely that the re-strengthening of anhydrite fault gouge through contact growth by pressure solution alone controls the long-term repeat frequency of earthquakes in the Apennines (cf. Marone(1998a)). Other possible causes for the longer recurrence times include the tectonic loading rates, the rate of pore fluid pressure build-up due to the natural CO_2 accumulation reported for the region (Chiodini et al., 2004; Collettini et al., 2009; Trippetta et al., 2013) or the frictional properties of other lithologies, such as the calcite and/or dolomite fault gouges present in the area (Carpenter et al., 2014; De Paola et al., 2008; Tesei et al., 2014). However, assuming that similar β values
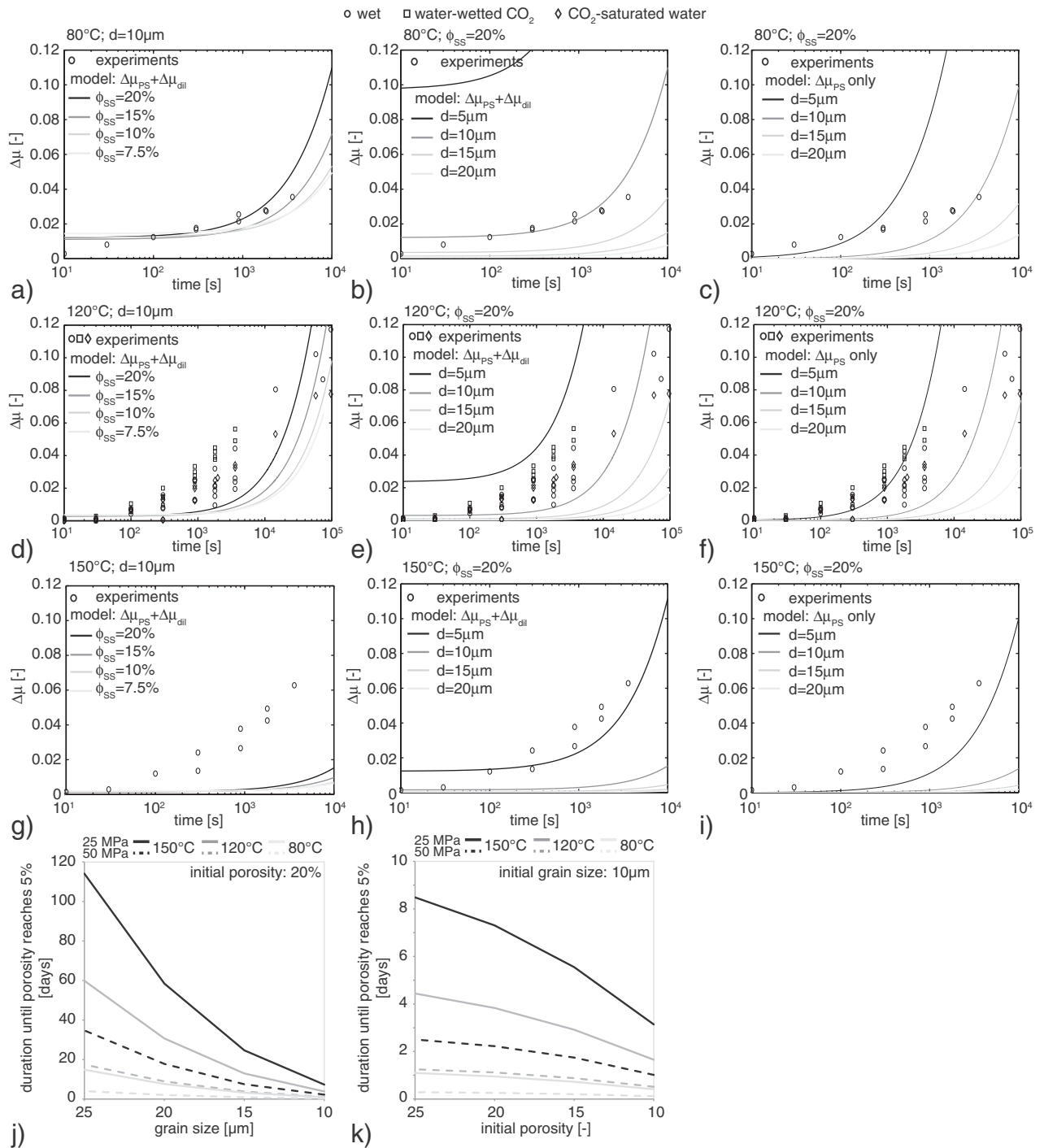
Fig. 11. Modeled re-strengthening and measured re-strengthening vs. time. a) Grain size of 10 μm at 80 °C, with different steady state sliding porosities. b) Steady state sliding porosity of 20% at 80 °C, different grain sizes. c) Steady state sliding porosity of 20% at 80 °C, different grain sizes, omitting all dilatational work. d) Grain size of 10 μm at 120 °C, different steady state sliding porosities. e) Steady state sliding porosity of 20% at 120 °C, different grain sizes. f) Steady state sliding porosity of 20% at 120 °C, different grain sizes, omitting all dilatational work. g) Grain size of 10 μm at 150 °C, different steady state sliding porosities. h) Steady state sliding porosity of 20% at 150 °C, different grain sizes. i) Steady state sliding porosity of 20% at 150 °C, different grain sizes, omitting all dilatational work. j) Duration until a porosity of 5% is reached, as a function of grain size (assuming a porosity of 20%). k) Duration until a porosity of 5% is reached, as a function of initial porosity (assuming a grain size of 10 μm). The time it takes to reach this 5% porosity represents a maximum time during which pressure solution is able to create new grain contact area, and these graphs indicate when healing through this mechanism is 'complete'.

indicate similar healing potentials (see Fig. 4) would imply that pure calcite gouges in the region should be fully healed as well (Carpenter et al., 2014).

Now, with respect to the possible effects of CO_2 penetration into anhydrite-bearing reservoir-bounding faults, all results so far indicate that, excluding any (long-term) mineral reactions, CO_2 itself does not exert a major influence on the frictional behavior of dry and wet

anhydrite fault gouges. What our results clearly illustrate though, is that CO_2 may act as an effective transport agent for small amounts of water. The small amounts of water present in our samples that contain water-wetted CO_2 lead to fault healing, velocity dependence and frictional strength as if the gouge was fully wet. Note that wet gouges with and without CO_2 all exhibit little to no seismogenic potential at the used in-situ stress of 25 MPa, comparable to a stress expected at a

depth of ~3 km. For wet anhydrite gouges there is some data to indicate that an increase in normal stress from 10 to 30 MPa may lead to a slight decrease in $(a-b)$ values (Scuderi et al., 2013). Long-term CO_2 injection will most likely lead to a chimney of relatively dry (supercritical) CO_2, surrounded by progressively wetter CO_2 (Johnson et al., 2004; Rochelle et al., 2004). Since CO_2 can only take up small amounts of water before it is saturated (Duan and Sun, 2003), in order to fully dry out a (previously wet) fault zone, a significant flux of CO_2 undersaturated with respect to water would be needed. In a CO_2 sequestration scenario, a site should be chosen with a high (expected) probability of being leak-free, which should render the occurrence of such a flux unlikely – especially since proximity to detectable fault zones can easily be avoided by careful planning. This implies that the velocity-weakening as displayed by our dry samples should thus be relatively easy to avoid as well. However, in a naturally CO_2 degassing environment such as the Italian Apennines (e.g. Chiodini et al., 2004; Collettini et al., 2008; Mirabella et al., 2008), faults are known to be permeable fluid pathways (e.g. Annunziatellis et al., 2008), for which such a desiccation-scenario may not be so easily discarded, since high CO_2 fluxes pass through the fault zone. In such a scenario, fault zone desiccation by CO_2 may lead to a change in the frictional stability of the fault zone as it dries out over time. If this were the case, desiccation may also slow down healing, since dry samples exhibit a factor 5–20 less re-strengthening than wet samples, possibly explaining longer fault recurrence times, and possibly even associated with time-dependent desiccation of the fault zone. For the Apennines however, the field evidence seems to suggest that fault zones still contained water at depth (Collettini et al., 2009; De Paola et al., 2008).

5. Conclusions

We have performed slide–hold–slide experiments on simulated anhydrite fault gouge, where a sequence of slide–hold–slides was followed by a velocity-stepping sequence. We have compared the velocity-dependence of friction in these experiments to that in experiments during which no holds occurred. We have investigated the influence of temperature, as the well as the effect of the presence or absence of water and/or CO_2. We can conclude the following:

1) Dry samples tested under vacuum show measurable healing and stress relaxation at all investigated temperatures (22 °C–150 °C), with a factor 5 to 20 less healing than wet samples. Dry samples are inferred to heal by plastic asperity creep ("Dieterich-type healing").
2) Wet samples are inferred to heal by an increase in contact area and packing density due to compaction by pressure solution creep, possibly enhanced by fault gouge localization. In addition, we observed an increase in steady state sliding strength for hold periods of 60 min or more, interpreted to be related to a (pressure solution induced) increase in cohesion.
3) Dry samples show velocity-weakening behavior at temperature of 120 °C and higher, where the presence of holds slightly decreases $(a-b)$-values. This decrease is correlated with decreased a-values, postulated to be related to local re-strengthening and an associated increase in localization.
4) Wet samples show slightly more marked velocity strengthening behavior when increasing the temperature from 80 to 150 °C, even though a and b values decrease over the same temperature interval. There is no visible effect on $(a-b)$ from the presence of hold periods. The decrease in a and b is assumed to be related to the decreased effectiveness of pressure solution or to an increase in localization.
5) On the time-scale of these experiments CO_2 neither influences anhydrite healing behavior nor the velocity-dependence of friction. Samples pressurized with water-wetted CO_2 show similar behavior to fully wet samples, which is inferred to be related to CO_2 acting as an effective transport agent for water. This may lead to nanometer-

thick water films coating the grains, thus enabling pressure solution.
6) Using a rate model for pressure solution to model the healing of anhydrite gouges by assuming it is caused by an increase in contact area by pressure solution only, we are able to explain part of the results for wet samples. An increase in gouge cohesion must play some role as well. Extrapolation of the pressure solution model to the low porosity of 5% indicates that the maximum re-strengthening of anhydrite fault gouges through such a mechanism can only take days to tens of days. Such a mechanism can thus not explain the recurrence time of M ≥ 6 earthquakes occurring in the Italian Apennines.
7) Assuming that faults in natural settings are wet, our results show little seismogenic potential for anhydrite-bearing faults. Furthermore, since only small amounts of water are needed to generate velocity-strengthening behavior, it seems unlikely that CO_2 stored in a subsurface reservoir will fully desiccate a reservoir-bounding fault zone, especially since careful planning can help to avoid proximity of the injection well to the fault zone.

Appendix A. Supplementary data

Supplementary data to this article can be found online at http://dx.doi.org/10.1016/j.tecto.2015.06.012.

References

Alsharhan, A.S., Nairn, A.E.M., 1994. The late Permian carbonates (Khuff Formation) in the western Arabian Gulf: its hydrocarbon parameters and paleogeographical aspects. Carbonates Evaporites 9, 132–142. http://dx.doi.org/10.1007/BF03175226.

Annunziatellis, A., Beaubien, S., Bigi, S., Ciotoli, G., Coltella, M., Lombardi, S., 2008. Gas migration along fault systems and through the vadose zone in the Latera caldera (central Italy): implications for CO_2 geological storage. Int. J. Greenhouse Gas Control 2, 353–372. http://dx.doi.org/10.1016/j.ijggc.2008.02.003.

Bai, G., Xu, Y., 2014. Giant fields retain dominance in reserves growth. Oil Gas J. 112.

Barchi, M.R., Mirabella, F., 2009. The 1997–98 Umbria–Marche earthquake sequence: "geological" vs. "seismological" faults. Tectonophysics 476, 170–179. http://dx.doi.org/10.1016/j.tecto.2008.09.013.

Beeler, N.M., Tullis, T.E., Weeks, J.D., 1994. The roles of time and displacement in the evolution effect in rock friction. Geophys. Res. Lett. 21, 1987–1990. http://dx.doi.org/10.1029/94GL01599.

Beeler, N.M., Tullis, T.E., Blanpied, M.L., Weeks, J.D., 1996. Frictional behavior of large displacement experimental faults. J. Geophys. Res. 101, 8697–8715. http://dx.doi.org/10.1029/96JB00411.

Benson, S., Cook, P., 2005. Special IPCC Report on Carbon Dioxide Capture and Storage, Working Group III of the Intergovernmental Panel on Climate Change. Cambridge University Press, Cambridge and New York.

Blanpied, M.L., Marone, C., Lockner, D.A., Byerlee, J.D., King, D.P., 1998. Quantitative measure of the variation in fault rheology due to fluid–rock interactions. J. Geophys. Res. 103, 9691. http://dx.doi.org/10.1029/98JB00162.

Blount, C.W., Dickson, F.W., 1969. The solubility of anhydrite ($CaSO_4$) in NaCl–H_2O from 100 to 450 °C and 1 to 1000 bars. Geochim. Cosmochim. Acta 33, 227–245. http://dx.doi.org/10.1016/0016-7037(69)90140-9.

Bos, B., Spiers, C.J., 2000. Effect of phyllosilicates on fluid-assisted healing of gouge-bearing faults. Earth Planet. Sci. Lett. 184, 199–210. http://dx.doi.org/10.1029/2001JB000301.

Bos, B., Spiers, C.J., 2002. Fluid-assisted healing processes in gouge-bearing faults: insights from experiments on a rock analogue system. Pure Appl. Geophys. 159, 2537–2566. http://dx.doi.org/10.1029/2001JB000301.

Byerlee, J., Summers, R., 1976. A note on the effect of fault gouge thickness on fault stability. Int. J. Rock Mech. Min. Sci. Geomech. Abstr. 13, 35–36. http://dx.doi.org/10.1016/0148-9062(76)90226-6.

Carpenter, B.M., Scuderi, M.M., Collettini, C., Marone, C., 2014. Frictional heterogeneities on carbonate-bearing normal faults: insights from the Monte Maggio Fault, Italy. J. Geophys. Res. Solid Earth http://dx.doi.org/10.1002/2014JB011337 (n/a–n/a).

Cello, G., Mazzoli, S., Tondi, E., Turco, E., 1997. Active tectonics in the central Apennines and possible implications for seismic hazard analysis in peninsular Italy. Tectonophysics 272, 43–68. http://dx.doi.org/10.1016/S0040-1951(96)00275-2.

Chang, R., 2000. Physical Chemistry for the Chemical and Biological Sciences. University Science Books, Sausalito, California.

Chester, F.M., Higgs, N.G., 1992. Multimechanism friction constitutive model for ultrafine quartz gouge at hypocentral conditions. J. Geophys. Res. Solid Earth 97, 1859–1870. http://dx.doi.org/10.1029/91JB02349.

Chiodini, G., Cardellini, C., Amato, A., Boschi, E., Caliro, S., Frondini, F., Ventura, G., 2004. Carbon dioxide Earth degassing and seismogenesis in central and southern Italy. Geophys. Res. Lett. 31, L07615. http://dx.doi.org/10.1029/2004gl019480.

Collettini, C., Barchi, M.R., 2002. A low-angle normal fault in the Umbria region (Central Italy): a mechanical model for the related microseismicity. Tectonophysics 359, 97–115.

Collettini, C., Cardellini, C., Chiodini, G., De Paola, N., Holdsworth, R.E., Smith, S.A.F., 2008. Fault weakening due to CO_2 degassing in the Northern Apennines: short- and long-term processes. Geol. Soc. Lond. Spec. Publ. 299, 175–194. http://dx.doi.org/10.1144/sp299.11.

Collettini, C., De Paola, N., Faulkner, D.R., 2009. Insights on the geometry and mechanics of the Umbria–Marche earthquakes (Central Italy) from the integration of field and laboratory data. Tectonophysics 476, 99–109. http://dx.doi.org/10.1016/j.tecto.2008.08.013.

De Meer, S., Spiers, C.J., 1999. Influence of pore-fluid salinity on pressure solution creep in gypsum. Tectonophysics 308, 311–330.

De Paola, N., Collettini, C., Faulkner, D.R., Trippetta, F., 2008. Fault zone architecture and deformation processes within evaporitic rocks in the upper crust. Tectonics 27, TC4017. http://dx.doi.org/10.1029/2007tc002230.

Dell'Angelo, L.N., Olgaard, D.L., 1995. Experimental deformation of fine-grained anhydrite: evidence for dislocation and diffusion creep. J. Geophys. Res. 100, 15425–15440. http://dx.doi.org/10.1029/95jb00956.

Dieterich, J.H., 1972. Time-dependent friction in rocks. J. Geophys. Res. 77, 3690–3697. http://dx.doi.org/10.1029/JB077i020p03690.

Dieterich, J.H., 1978. Time-dependent friction and the mechanics of stick–slip. Pure Appl. Geophys. 116, 790–806. http://dx.doi.org/10.1007/BF00876539.

Dieterich, J.H., 1979. Modeling of rock friction: 1. Experimental results and constituve equations. J. Geophys. Res. 84, 2161–2168. http://dx.doi.org/10.1029/JB084iB05p02161.

Dieterich, J.H., Conrad, G., 1984. Effect of humidity on time- and velocity-dependent friction in rocks. J. Geophys. Res. 89, 4196. http://dx.doi.org/10.1029/JB089iB06p04196.

Dieterich, J.H., Kilgore, B.D., 1994. Direct observation of frictional contacts: new insights for state-dependent properties. Pure Appl. Geophys. 143, 283–302. http://dx.doi.org/10.1007/BF00874332.

Duan, Z., Sun, R., 2003. An improved model calculating CO_2 solubility in pure water and aqueous NaCl solutions from 273 to 533 K and from 0 to 2000 bar. Chem. Geol. 193, 257–271. http://dx.doi.org/10.1016/S0009-2541(02)00263-2.

Engelder, J.T., 1974. Cataclasis and the generation of fault gouge. Geol. Soc. Am. Bull. 85, 1515–1522. http://dx.doi.org/10.1130/0016-7606(1974)85<1515:catgof>2.0.co;2.

Frye, K.M., Marone, C., 2002. Effect of humidity on granular friction at room temperature. J. Geophys. Res. 107, 2309. http://dx.doi.org/10.1029/2001JB000654.

Galli, P., Galadini, F., Pantosti, D., 2008. Twenty years of paleoseismology in Italy. Earth Sci. Rev. 88, 89–117. http://dx.doi.org/10.1016/j.earscirev.2008.01.001.

Geluk, M.C., 2000. Late Permian (Zechstein) carbonate-facies maps the Netherlands. Geol. Mijnb./Neth. J. Geosci. 79, 17–27.

Geluk, M.C., 2007. Permian, Geology of the Netherlands. Royal Netherlands Academy of Arts and Sciences, Amsterdam, Netherlands.

Gratier, J.-P., Dysthe, D., Renard, F., 2013. The role of pressure solution creep in the ductility of the earth's upper crust. Adv. Geophys. 54, 47–179. http://dx.doi.org/10.1016/B978-0-12-380940-7.00002-0.

Hangx, S.J.T., Spiers, C.J., Peach, C.J., 2010. Mechanical behavior of anhydrite caprock and implications for CO_2 sealing capacity. J. Geophys. Res. 115, B07402. http://dx.doi.org/10.1029/2009jb006954.

Hangx, S.J.T., Pluymakers, A., ten Hove, A., Spiers, C.J., 2014. Effects of lateral variations in rock composition and texture on anhydrite caprock integrity of CO_2 storage systems. Int. J. Rock Mech. Min. Sci. 69, 80–92. http://dx.doi.org/10.1016/j.ijrmms.2014.03.001.

Hickman, S.H., Evans, B., 1992. Growth of Grain Contacts in Halite by Solution-transfer: Implications for Diagenesis, Lithification and Strength Recovery. In: Evans, B., Wong, T. (Eds.), Fault Mechanics and Transport Properties of Rocks. Academic Press, London, pp. 253–280.

Hildyard, R.C., Prior, D.J., Mariani, E., Faulkner, D.R., 2011. Characterization of microstructures and interpretation of flow mechanisms in naturally deformed, fine-grained anhydrite by means of EBSD analysis. Geol. Soc. Lond. Spec. Publ. 360, 237–255. http://dx.doi.org/10.1144/sp360.14.

Hummel, W., Berner, U., Curti, E., Pearson, F.J., Thoenen, T., 2002. Chemical Thermodynamic Database 01/01. Nagra/PSI.

Ikari, M.J., Saffer, D.M., Marone, C., 2009. Frictional and hydrologic properties of clay-rich fault gouge. J. Geophys. Res. 114, B05409. http://dx.doi.org/10.1029/2008JB006089.

Johnson, T., 1981. Time-dependent friction of granite: implications for precursor slip on faults. J. Geophys. Res. 86, 6017. http://dx.doi.org/10.1029/JB086iB07p06017.

Johnson, J.W., Nitao, J.J., Knauss, K.G., 2004. Reactive transport modelling of CO_2 storage in saline aquifers to elucidate fundamental processes, trapping mechanisms and

sequestration partitioning. Geol. Soc. Lond. Spec. Publ. 233, 107–128. http://dx.doi.org/10.1144/GSL.SP.2004.233.01.08.

Karner, S.L., Marone, C., 1998. The effect of shear load on frictional healing in simulated fault gouge. Geophys. Res. Lett. 25, 4561–4564. http://dx.doi.org/10.1029/1998GL900182.

Kwak, J.H., Hu, J.Z., Hoyt, D.W., Sears, J.A., Wang, C., Rosso, K.M., Felmy, A.R., 2010. Metal carbonation of forsterite in supercritical CO_2 and H_2O using solid state ^{29}Si, ^{13}C NMR spectroscopy. J. Phys. Chem. C 114, 4126–4134. http://dx.doi.org/10.1021/jp1001308.

Lehner, F.K., 1995. A model for intergranular pressure solution in open systems. Tectonophysics 245, 153–170. http://dx.doi.org/10.1016/0040-1951(94)00232-X.

Loring, J.S., Thompson, C.J., Wang, Z., Joly, A.G., Sklarew, D.S., Schaef, H.T., Ilton, E.S., Rosso, K.M., Felmy, A.R., 2011. In situ infrared spectroscopic study of forsterite carbonation in wet supercritical CO_2. Environ. Sci. Technol. 45, 6204–6210. http://dx.doi.org/10.1021/es201284e.

Marone, C., 1998a. The effect of loading rate on static friction and the rate of fault healing during the earthquake cycle. Nature 391, 69–72. http://dx.doi.org/10.1038/34157.

Marone, C., 1998b. Laboratory-derived friction laws and their application to seismic faulting. Annu. Rev. Earth Planet. Sci. 26, 643–696. http://dx.doi.org/10.1146/annurev.earth.26.1.643.

Marone, C., Cox, S.J.D., 1994. Scaling of rock friction constitutive parameters: the effects of surface roughness and cumulative offset on friction of gabbro. Pure Appl. Geophys. 143, 359–385. http://dx.doi.org/10.1007/BF00874335.

Marone, C., Raleigh, C.B., Scholz, C.H., 1990. Frictional behavior and constitutive modeling of simulated fault gouge. J. Geophys. Res. 95, 7007–7025. http://dx.doi.org/10.1029/JB095iB05p07007.

Miocic, J.M., Gilfillan, S.M.V., McDermott, C., Haszeldine, R.S., 2013. Mechanisms for CO_2 leakage prevention: a global dataset of natural analogues. Energy Procedia 40, 320–328. http://dx.doi.org/10.1016/j.egypro.2013.08.037.

Mirabella, F., Barchi, M.R., Lupattelli, A., 2008. Seismic reflection data in the Umbria Marche Region: limits and capabilities to unravel the subsurface structure in a seismically active area. Ann. Geophys. 51. http://dx.doi.org/10.4401/ag-3032.

Muhuri, S.K., Dewers, T.A., Scott, T.E., Reches, Z., 2003. Interseismic fault strengthening and earthquake-slip instability: friction or cohesion? Geology 31, 881–884. http://dx.doi.org/10.1130/g19601.1.

Müller, P., Siemes, H., 1974. Festigkeit, verformbarkeit und gefügeregelung von anhydrit — experimentelle stauchverformung unter manteldrucken bis 5 kbar bei temperaturen bis 300 °C. Tectonophysics 23, 105–127. http://dx.doi.org/10.1016/0040-1951(74)90114-0.

Müller, W.H., Schmid, S.M., Briegel, U., 1981. Deformation experiments on anhydrite rocks of different grain sizes: rheology and microfabric. Tectonophysics 78, 527–543. http://dx.doi.org/10.1016/0040-1951(81)90027-5.

Nakatani, M., Scholz, C.H., 2004. Frictional healing of quartz gouge under hydrothermal conditions: 1. Experimental evidence for solution transfer healing mechanism. J. Geophys. Res. 109, B07201. http://dx.doi.org/10.1029/2001jb001522.

Niemeijer, A.R., Collettini, C., 2013. Frictional properties of a low-angle normal fault under in situ conditions: thermally-activated velocity weakening. Pure Appl. Geophys. http://dx.doi.org/10.1007/s00024-013-0759-6.

Niemeijer, A.R., Spiers, C.J., 2006. Velocity dependence of strength and healing behaviour in simulated phyllosilicate-bearing fault gouge. Tectonophysics 427, 231–253. http://dx.doi.org/10.1016/j.tecto.2006.03.048.

Niemeijer, A.R., Spiers, C.J., 2007. A microphysical model for strong velocity weakening in phyllosilicate-bearing fault gouges. J. Geophys. Res. 112, B10405. http://dx.doi.org/10.1029/2007jb005008.

Niemeijer, A.R., Vissers, R.L.M., 2014. Earthquake rupture propagation inferred from the spatial distribution of fault rock frictional properties. Earth Planet. Sci. Lett. 396, 154–164. http://dx.doi.org/10.1016/j.epsl.2014.04.010.

Niemeijer, A., Marone, C., Elsworth, D., 2008. Healing of simulated fault gouges aided by pressure solution: results from rock analogue experiments. J. Geophys. Res. 113, B04204. http://dx.doi.org/10.1029/2007jb005376.

Olsen, M.P., Scholz, C.H., Léger, A., 1998. Healing and sealing of a simulated fault gouge under hydrothermal conditions: implications for fault healing. J. Geophys. Res. 103, 7421. http://dx.doi.org/10.1029/97JB03402.

Palumbo, L., Benedetti, L., Bourles, D., Cinque, A., Finkel, R., 2004. Slip history of the Magnola fault (Apennines, Central Italy) from ^{36}Cl surface exposure dating: evidence for strong earthquakes over the Holocene. Earth Planet. Sci. Lett. 225, 163–176. http://dx.doi.org/10.1016/j.epsl.2004.06.012.

Pantosti, D., Schwartz, D.P., Valensise, G., 1993. Paleoseismology along the 1980 surface rupture of the Irpinia Fault: implications for earthquake recurrence in the southern Apennines, Italy. J. Geophys. Res. 98, 6561–6577. http://dx.doi.org/10.1029/92jb02277.

Pluymakers, A., Spiers, C.J., 2014. Compaction creep of simulated anhydrite fault gouge by pressure solution: theory vs. experiments and implications for fault sealing. Geol. Soc. Lond. Spec. Publ. http://dx.doi.org/10.1144/SP409.6.

Pluymakers, A., Peach, C.J., Spiers, C.J., 2014a. Diagenetic compaction experiments on simulated anhydrite fault gouge under static conditions. J. Geophys. Res. B5, 4123–4148. http://dx.doi.org/10.1002/2014JB011073.

Pluymakers, A., Samuelson, J.E., Niemeijer, A.R., Spiers, C.J., 2014. Effects of temperature and CO_2 on the frictional behavior of simulated anhydrite fault rock. J. Geophys. Res. Solid Earth 119 120, 8728–8747. http://dx.doi.org/10.1002/2014JB011575.

Raj, R., 1982. Creep in polycrystalline aggregates by matter transport through a liquid phase. J. Geophys. Res. 87, 4731–4739. http://dx.doi.org/10.1029/JB087iB06p04731.

Reinen, L.A., Weeks, J.D., 1993. Determination of rock friction constitutive parameters using an iterative least squares inversion method. J. Geophys. Res. 98, 15937. http://dx.doi.org/10.1029/93JB00780.

Renard, F., Beauprêtre, S., Voisin, C., Zigone, D., Candela, T., Dysthe, D.K., Gratier, J.-P., 2012. Strength evolution of a reactive frictional interface is controlled by the dynamics of contacts and chemical effects. Earth Planet. Sci. Lett. 341–344, 20–34. http://dx.doi.org/10.1016/j.epsl.2012.04.048.

Rochelle, C.A., Czernichowski-Lauriol, I., Milodowski, A.E., 2004. The impact of chemical reactions on CO_2 storage in geological formations: a brief review. Geol. Soc. Lond. Spec. Publ. 233, 87–106. http://dx.doi.org/10.1144/GSL.SP.2004.233.01.07.

Ruina, A., 1983. Slip instability and state variable friction laws. J. Geophys. Res. 88, 10359–10370.

Rutqvist, J., Rinaldi, A.P., Cappa, F., Moridis, G.J., 2013. Modeling of fault reactivation and induced seismicity during hydraulic fracturing of shale-gas reservoirs. J. Pet. Sci. Eng. 107, 31–44. http://dx.doi.org/10.1016/j.petrol.2013.04.023.

Rutter, E.H., 1976. The kinetics of rock deformation by pressure solution. Philos. Trans. R. Soc. Lond. Ser. A Math. Phys. Sci. 283, 203–219. http://dx.doi.org/10.1098/rsta.1976.0079.

Rutter, E.H., 1983. Pressure solution in nature, theory and experiment. J. Geol. Soc. Lond. 140, 725–740. http://dx.doi.org/10.1144/gsjgs.140.5.0725.

Saffer, D.M., Marone, C., 2003. Comparison of smectite- and illite-rich gouge frictional properties: application to the updip limit of the seismogenic zone along subduction megathrusts. Earth Planet. Sci. Lett. 215, 219–235. http://dx.doi.org/10.1016/S0012-821X(03)00424-2.

Samuelson, J., Spiers, C.J., 2012. Fault friction and slip stability not affected by CO_2 storage: evidence from short-term laboratory experiments on North Sea reservoir sandstones and caprocks. Int. J. Greenhouse Gas Control 11, S78–S90. http://dx.doi.org/10.1016/j.ijggc.2012.09.018 (Supple).

Scholz, C.H., 2002. The Mechanics of Earthquakes and Faulting. Cambridge University Press, Cambridge.

Scholz, C.H., Engelder, J.T., 1976. The role of asperity indentation and ploughing in rock friction–II: influence of relative hardness and normal load. Int. J. Rock Mech. Min. Sci. Geomech. Abstr. 13, 155–163.

Scuderi, M.M., Niemeijer, A.R., Collettini, C., Marone, C., 2013. Frictional properties and slip stability of active faults within carbonate–evaporite sequences: the role of dolomite and anhydrite. Earth Planet. Sci. Lett. 369-370, 220–232. http://dx.doi.org/10.1016/j.epsl.2013.03.024.

Scuderi, M.M., Carpenter, B.M., Marone, C., 2014. Physicochemical processes of frictional healing: effects of water on stick–slip stress drop and friction of granular fault gouge. J. Geophys. Res. Solid Earth 119. http://dx.doi.org/10.1002/2013JB010641 (n/a-n/a).

Spiers, C.J., Schutjens, P.T.M., 1990. Densification of crystalline aggregates by fluid-phase diffusional creep. In: Barber, D.J., Meredith, P.G. (Eds.), Deformation Processes in Minerals, Ceramics and Rocks. Unwin Hyman Ltd, London.

Spiers, C.J., De Meer, S., Niemeijer, A.R., Zhang, X., 2004. Kinetics of rock deformation by pressure solution and the role of thin aqueous films. In: Nakashima, S., Spiers, C.J., Mercury, L, Fenter, P.A., Hochella Jr., M.F. (Eds.), Physicochemistry of Water in Geological and Biological Systems — Structures and Properties of Thin Aqueous Films. Universal Academy Press, Inc., Tokyo, pp. 129–158.

Tenthorey, E., Cox, S.F., 2006. Cohesive strengthening of fault zones during the interseismic period: an experimental study. J. Geophys. Res. Solid Earth 111, B09202. http://dx.doi.org/10.1029/2005jb004122.

Tenthorey, E., Cox, S.F., Todd, H.F., 2003. Evolution of strength recovery and permeability during fluid–rock reaction in experimental fault zones. Earth Planet. Sci. Lett. 206, 161–172. http://dx.doi.org/10.1016/S0012-821X(02)01082-8.

Tesei, T., Collettini, C., Barchi, M.R., Carpenter, B.M., Di Stefano, G., 2014. Heterogeneous strength and fault zone complexity of carbonate-bearing thrusts with possible implications for seismicity. Earth Planet. Sci. Lett. 408, 307–318. http://dx.doi.org/10.1016/j.epsl.2014.10.021.

Thoenen, T., Kulik, D., 2003. Chemical thermodynamical database 01/01 for the GEM-Selektor (V.2-PSI). Geochemical Model. code.

Trippetta, F., Collettini, C., Barchi, M.R., Lupattelli, A., Mirabella, F., 2013. A multidisciplinary study of a natural example of a CO_2 geological reservoir in central Italy. Int. J. Greenhouse Gas Control 12, 72–83. http://dx.doi.org/10.1016/j.ijggc.2012.11.010.

Verberne, B.A., de Bresser, J.H.P., Niemeijer, A.R., Spiers, C.J., de Winter, D.A.M., Plümper, O., 2013a. Nanocrystalline slip zones in calcite fault gouge show intense crystallographic preferred orientation: crystal plasticity at sub-seismic slip rates at 18–150 °C. Geology G34279, 1. http://dx.doi.org/10.1130/g34279.1.

Verberne, B.A., Spiers, C.J., Niemeijer, A., De Bresser, J.H.P., De Winter, D.A.M., Plümper, O., 2013b. Frictional properties and microstructures of calcite-rich fault gouges sheared at subseismic sliding velocities. Pure Appl. Geophys. 1–24. http://dx.doi.org/10.1007/s00024-013-0760-0.

Verberne, B.A., Plümper, O., de Winter, D.A.M., Spiers, C.J., 2014. Superplastic nanofibrous slip zones control seismogenic fault friction. Science 346, 1342–1344. http://dx.doi.org/10.1126/science.1259003.

Weeks, J.D., Tullis, T.E., 1985. Frictional sliding of dolomite: a variation in constitutive behavior. J. Geophys. Res. 90, 7821. http://dx.doi.org/10.1029/JB090iB09p07821.

Weyl, P.K., 1959. Pressure solution and the force of crystallization: a phenomenological theory. J. Geophys. Res. 64, 2001–2025. http://dx.doi.org/10.1029/JZ064i011p02001.

Yasuhara, H., Marone, C., Elsworth, D., 2005. Fault zone restrengthening and frictional healing: the role of pressure solution. J. Geophys. Res. Solid Earth 110, B06310. http://dx.doi.org/10.1029/2004jb003327.

Zhang, X., Spiers, C.J., Peach, C.J., 2010. Compaction creep of wet granular calcite by pressure solution at 28 °C to 150 °C. J. Geophys. Res. 115, B09217. http://dx.doi.org/10.1029/2008jb005853.